

Ballistic phonon imaging in sapphire: Bulk focusing and critical-cone channeling effects

A. G. Every,* G. L. Koos, and J. P. Wolfe

Physics Department and Materials Research Laboratory, University of Illinois at Urbana—Champaign, Urbana, Illinois 61801

(Received 17 August 1983)

Phonon imaging has been used to study the anisotropy of ballistic phonon flux in single crystals of sapphire cut in several different crystallographic orientations. Three types of intense local maxima in phonon flux are observed in these images. The most prominent of these structure types corresponds to mathematical singularities in bulk phonon focusing. The second type of structure, which has not been noted in previous phonon-imaging experiments, is a nonsingular local maximum in flux which can be quite sharp, and would evolve into a genuine singularity if the elastic constants were appropriately changed. These “precursors” and the singularity structures are well predicted in sapphire by Monte Carlo simulations based on the low-temperature elastic constants. The third type of structure is intrinsic to the surfaces of the sapphire and is sensitive to the crystallographic orientation and the quality of these surfaces. It corresponds to a concentration of transverse phonons close to the critical cone for mode conversion between transverse and longitudinal waves at the surface. We interpret this wave-vector channeling effect in terms of a longitudinal pseudo-surface-wave that exists at the sapphire surface when it is either free or only weakly perturbed by an adjoining medium. In our experiments the adjoining medium is a metal film. A model for treating weak mechanical bonding between two adjacent media is developed which is able to account qualitatively for the width and intensities of the observed critical-cone structures. The existence of these new surface-related structures signifies the potential usefulness of phonon imaging for characterizing the scattering of thermal phonons at interfaces. In particular, our results provide a quantitative measure of the elastic coupling between crystal and metal film. The weak nature of this coupling helps to explain previously reported anomalous Kapitza resistance and phonon reflectivity of solid-solid interfaces.

I. INTRODUCTION

Phonon-imaging techniques have been used successfully in recent years in studying the complex directional dependence of ballistic phonon transport in crystals at low temperatures.¹⁻⁴ In the typical phonon-imaging experiment a point source of heat (generated by means of a focused laser or an electron beam) is scanned across the metallized face of a crystal, and ballistic phonons emanating from this heated spot are detected by a superconducting bolometer mounted on the opposite face of the crystal. The images that are generated in this way reveal pronounced nonuniformity in phonon flux, and they invariably feature sharp, well-defined structures corresponding to directions in which the phonon flux is very much greater than that in the background.

In the past the principal cause of flux anisotropy has been ascribed to a bulk effect known as phonon focusing,⁵ whereby, in a crystal, the wave vector \vec{k} and ray vector \vec{V} of a phonon are not, in general, colinear. As a consequence, even with the assumption that the phonons entering the crystal have \vec{k} vectors which are distributed uniformly in all forward directions, the concentration of phonon \vec{V} 's, and thus the energy flux, can vary enormously with direction.⁶⁻¹⁰ The phonon constant-frequency surface (slowness surface) is a useful construct in interpreting this effect. A ray vector $\vec{V} = \vec{\nabla}_{\vec{k}}\omega(\vec{k})$ is required to be

normal to this surface. A typical slowness surface (see, e.g., Fig. 2) displays regions of positive and negative Gaussian curvature and lines of zero curvature (parabolic lines) separating these different regions. The smaller the curvature of this surface at any point, the greater the extent to which ray vectors are grouped together in the direction normal to this surface, and hence the larger the flux enhancement in this direction. At the parabolic lines this focusing effect becomes mathematically infinite,^{2,11} thereby yielding a singularity (caustic) in the phonon-flux intensity. Phonon caustics have been calculated on the basis of continuum elasticity theory for a number of crystals, and these are in good agreement with the sharp structures that have been experimentally observed in phonon images of crystals in the past.

In this paper we provide a detailed description of the phonon-focusing patterns of sapphire (Al_2O_3), both from a theoretical and experimental point of view. These patterns conform to the trigonal symmetry (Laue rhombohedral group $R1$) of the sapphire crystal. One of our phonon images is shown in Fig. 1(a). As can be seen, it clearly displays the predicted pattern of caustics shown as the thin solid lines in Fig. 1(c). In addition, our images for sapphire contain two other types of well-defined structures. The first of these is comprised of the pair of sloping ridges running from the center to the lower corners of the experimental image in Fig. 1(a). This feature is predicted by bulk-focusing theory and corresponds to

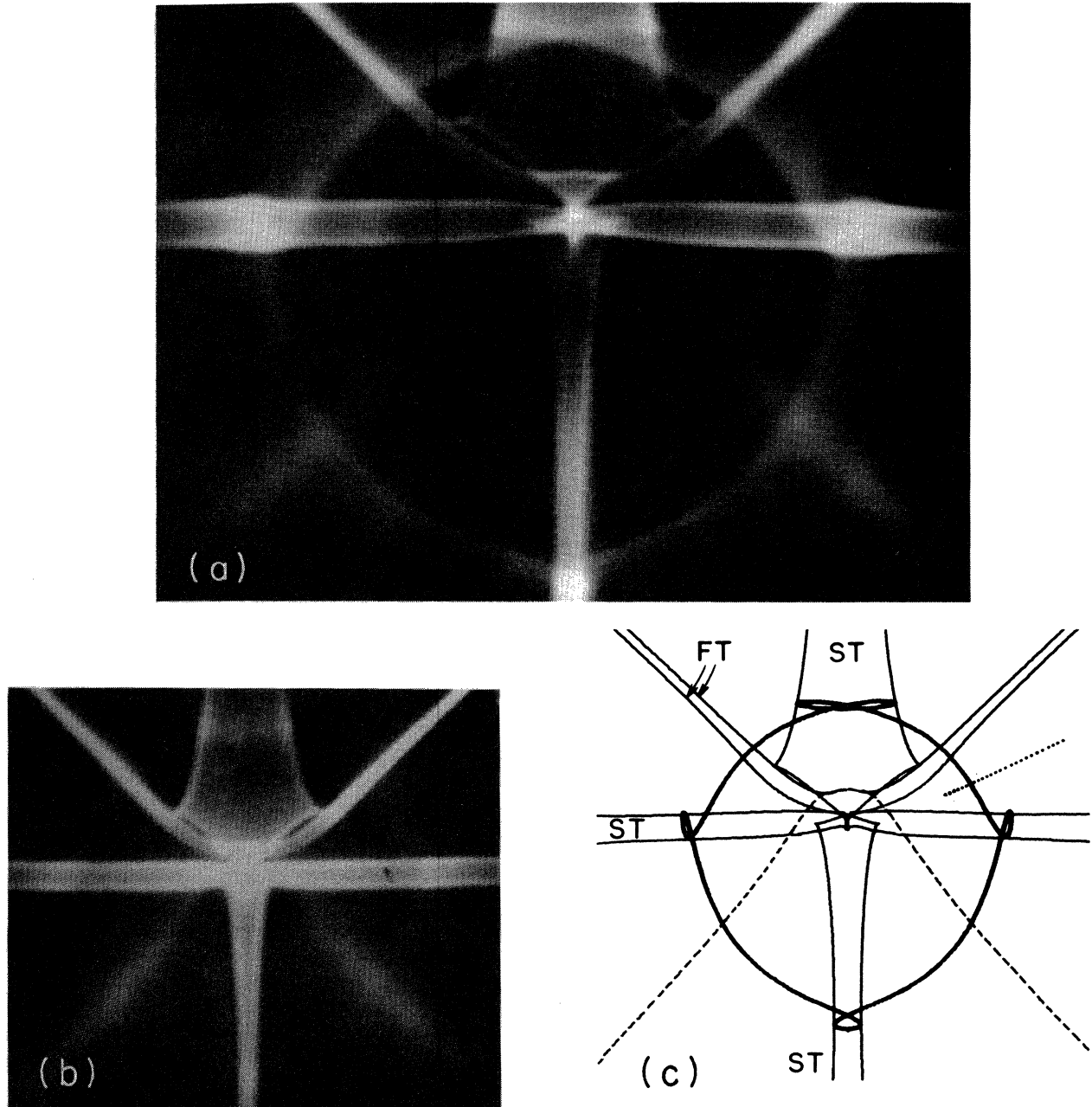


FIG. 1. (a) Ballistic phonon image for sapphire at 1.6 K. The detector and excitation faces are cut in the $[1\bar{1}02]$ direction, referred to conventional hexagonal axes, and both are highly polished. Bright regions indicate directions of high phonon flux. The image represents a $\pm 32^\circ$ horizontal scan with the $[1\bar{1}02]$ direction at the center of the pattern. The time gates of the boxcar integrator are set to accept the ST and FT modes. (b) Similar to (a) but with both faces of the sapphire roughened as described in the text (Sec. III). (c) Theoretical map of the caustics for sapphire projected onto the viewing surface of (a) and (b). The fast and slow transverse caustics are identified. The ST critical-cone channeling contour is given by the thick line. The scan line for Fig. 15 is indicated by the dotted line. The dashed line indicates the position of the precursor.

large but *not* mathematically infinite phonon flux and is indicated by the dashed line in Fig. 1(c). Slight changes in the elastic constants, however, can transform these ridges into genuine singularities. Similar features have also been observed in diamond¹² and quartz¹³ and are, we feel, sufficiently widespread to warrant closer attention and a specific label. Since they generally seem to precede the appearance of new caustics as the elastic constants are

varied, which in practice might be effected by the application of stress or a change in the temperature, etc., we call these features "precursors."

Bulk focusing is only one of several processes influencing the directional dependence of phonon flux. Phonons crossing the interface between the metal film, where they are generated or detected, and the crystal substrate are subject to whatever conditions prevail at this interface.

References 14 and 15 pose some important questions on this issue. Extensive calculations have been carried out on the basis of acoustic mismatch theory, i.e., in the framework of continuum elasticity theory and assuming perfectly bonded (welded contact) adjoining media.^{16,17} For some situations, these calculations predict fairly gentle variations of the transmitted flux with direction. Such features are not easily verified in detail, since there are other factors ($1/r^2$ falloff with distance, phonon scattering, etc.) that have a comparable effect. In other cases, particularly where acoustic mismatch is large and the crystal is highly anisotropic, much more pronounced surface-derived anisotropy is predicted.¹⁶ A possible reason why experimental surface directivity effects have not been reported for solid-solid interfaces in the past is that sufficiently smooth crystal faces have not been employed in phonon-imaging experiments. Surface roughness, on a scale that is large compared with the dominant thermal-phonon wavelengths, will have the effect of smearing out any surface directivity effect in accordance with the distribution of surface normals, and therefore no sharp features from this source should be observable. (Note, however, that bulk focusing does not suffer the same fate.)

The sapphire crystals that we have used for obtaining the phonon images displayed in this paper are optically polished disks with surface roughness on a scale of less than 100 Å.¹⁸ They have revealed for the first time the unambiguous presence of surface-derived anisotropy of phonon flux in crystals.¹⁹ An examination of Fig. 1(a) reveals a striking feature not predicted by bulk-focusing theory: This is the large oval-shaped band or halo that is twisted into four small loops where it passes through pairs of slow transverse (ST) caustics. Great simplification is effected by translating this halo into a \vec{k} -space distribution of ST phonons, thereby removing the distorting effect of bulk focusing. The loops are eliminated, and the \vec{k} -space distribution that results is found to be sharply peaked in directions lying very close to the critical cone for mode conversion of ST waves to longitudinal (L) waves at the crystal surface. The thick line in Fig. 1(c) represents the calculated locus of these critical ST rays projected onto the viewing surface, and comparison with Fig. 1(a) shows that this contour is in good agreement with the position of the experimental halo. In other sapphire crystals with different crystallographic orientations of the surface, this new feature does not, in general, resemble a halo, but in all cases its shape is accurately predicted by the critical-cone condition. Moreover, there is also an analogous critical-cone channeling structure for fast transverse (FT) phonons.

We will show in this paper that this channeling effect is associated with an angular resonance that occurs in the mode conversion of bulk T to evanescent L waves at the sapphire surface when the crystal is quasifree, i.e., either loosely bonded to the metal film, bonded to a metal film of low acoustic impedance, or both. This type of resonance is the signature of a pseudo-surface-wave, also known as a leaky surface wave. Ideal bonding between the two media (when the acoustic impedance of the metal film is large) leads to the almost complete extinction of these

pseudo-surface-waves and is not able to explain the intensity of the channeling structure. The pattern and intensity of the critical-cone channeling of phonons can, however, be qualitatively accounted for by admitting "flexible" boundary conditions that allow for the relative displacement of the two adjoining media at the interface. This model is also able to account for our experimental observation that the appearance of the channeling structure is quite insensitive to the type of metal used for the heater film, provided that adequate adhesion to the sapphire substrate is achieved.

II. PHONON IMAGING OF SAPPHIRE

A. Experimental

The experimental method in this work is modeled after the technique first used by Northrop and Wolfe on germanium.² To study the directional nature of ballistic phonons in crystals we produce a small heat pulse on one face of the crystal and detect the phonons, emanating from this spot, at the opposite face. The need for a large array of phonon detectors is eliminated by slowly scanning the heat source across the front surface and recording the detector signal for each source location. A full image of the phonon-flux pattern is stored in a computer and then displayed on a television monitor through a video interface.

The crystals used in this experiment were sapphire windows, or disks, 2–3 mm thick and of several crystallographic orientations. All crystal faces were optically polished on a fine diamond lap and then buffed in a chemical-mechanical polishing solution of Syton by the supplier.¹⁸ This produced a surface that was smooth to about 100 Å over several millimeters, as measured by dragging a diamond stylus of radius 2.5 μm over the surface. High surface quality is needed to observe the surface effects reported here.

The phonon detector used here is a 50×50 μm² superconducting Al bolometer evaporated through a special mask onto the sample. This mask is formed by scanning a focused, Q-switched yttrium aluminum garnet (YAG) laser beam across a 1-μm-thick sheet of stainless steel to cut the bolometer pattern. The Al bolometer is 600 Å thick and thus has a small heat capacity and response time on the order of 10 ns to incoming heat pulses.

The small size of the detector enables us to resolve features in the flux pattern down to one degree of arc on 3-mm-thick samples. The bolometer is cooled to approximately 1.6 K and current biased so that the Al film is halfway through its superconducting transition. Thus the bolometer becomes a sensitive and fast detector of heat, capable of fine angular resolution.

The heat source in these experiments is provided by focusing a 200-mW Ar⁺ laser beam down to 50-μm spot on a metal film, which has been evaporated onto the crystal. The 5145-Å light is modulated by an acousto-optic device to provide a 100-ns pulses at a repetition rate of 100 kHz. The film prevents direct excitation of the bolometer and provides a spatially localized Planck energy distribu-

tion of phonons with instantaneous temperature of approximately 10 K. This implies a peak intensity near 600 GHz or 100-Å wavelength. We have found that Al, Cu, and Ni films of 2000-Å thickness all result in very similar phonon images, although the optical absorptivity of the metal (which is largest for Ni) does affect the absolute intensity of the images. On the other hand, our images obtained with Ag are very weak and nonuniform in intensity, evidently because of poor adhesion between Ag and sapphire.

The resulting signal from the bolometer is amplified by a fast preamplifier and then averaged by a boxcar integrator gated to accept both transverse phonon modes. This averaged signal is sent to a Digital Equipment Corporation LSI-11/23 computer that records the signal level and the position of the laser spot in the form of a 256×256 array. The computer also controls the scanning of the laser spot across the face of the sample through two steering mirrors attached to precision galvanometers. The final 256×256 array can then be displayed on a video monitor for analysis. The experimental and theoretical images presented in this paper are photographs of this monitor.

B. Phonon focusing theory

Bulk elastic anisotropy has a dramatic influence on the ballistic propagation of phonons in crystals. While a number of factors are involved, the most important contribution comes from phonon focusing.⁵ This effect has been discussed by a number of authors,¹⁻¹¹ and so only a brief summary of the salient points is given here. The phonon flux emanating in any direction, from a point heat source, is directly proportional to the phonon amplification factor A for that direction.⁵ This is the factor by which differential solid angles in \vec{k} space are *reduced* when mapped into \vec{V} space, and consequently the factor by which phonon ray vectors become concentrated in direction compared with their \vec{k} vectors.

The ray vector, $\vec{V} = \vec{\nabla}_{\vec{k}} \omega(\vec{k})$, of a phonon is required to be normal to its surface of constant frequency $\omega(\vec{k})$ in \vec{k} space. In the long-wavelength limit, where phonon velocities are independent of frequency, the simple scale change $\vec{k} \rightarrow \vec{k}/\omega(\vec{k})$ has the effect of collapsing all the constant-frequency surfaces onto a single surface, known as the acoustic slowness surface.²⁰⁻²² The tendency of phonon ray vectors to group in any direction clearly is dependent on the curvature of the slowness surface, and in fact it can be shown that^{2,9,10}

$$A^{-1} = |S^3 V K|, \quad (1)$$

where $\vec{S} = \vec{k}/\omega(\vec{k})$ is the slowness vector and K is the Gaussian curvature of the slowness surface. Figure 2 shows the slowness surface of sapphire.²³ Because of elastic anisotropy this surface is noticeably nonspherical; there are regions where this surface is entirely convex, i.e., both of the principal curvatures are positive, and there are saddle-shaped regions where the two principal curvatures are of opposite sign. Along the lines of parabolic points that separate these different regions, the Gaussian curvature, which is the product of the two principal curvatures,

is zero. The phonon amplification factor therefore varies greatly with direction, and along the parabolic lines, where $A^{-1} = 0$, it becomes infinite, yielding the caustics shown, for example, in Fig. 1(c).

The ray surface of sapphire is shown in Fig. 3. It represents the locus of the extremities of ray vectors (group-velocity vectors) pointing out from the origin. It is multiply folded in a complex way. The folding edges are composed of \vec{V} 's corresponding to parabolic points on the slowness surface and therefore directions of infinite focusing. When projected onto a given viewing surface these folds yield the singularity lines or caustics in the phonon images. Within the folding system for each real-space direction there are several ray vectors, all in general associated with different \vec{k} -space directions.

A convenient method for predicting the overall phonon-flux pattern is to generate a large number of random directions in \vec{k} space, compute the group-velocity directions for each of these \vec{k} 's, and then project these rays onto the specific viewing surface. The density of ray vectors in a small region on the viewing surface is proportional to the phonon-flux intensity along that propagation direction. This Monte Carlo technique has been used, for instance, in generating the theoretical phonon images in Fig. 4(a), which applies to the same crystallographic orientation as the experimental image of Fig. 1(a). The utility of this technique is that it conveys information on the phonon flux in all directions and reveals the existence of not only genuine singularities but also nonsingular maxima in the phonon intensity. Comparative intensities of various features are also revealed in these Monte Carlo images.

C. Focusing effects in sapphire

Ballistic phonon images for *c*-cut sapphire, obtained by electron-beam excitation, have recently been reported by Eichele, Huebener, and Siefert in Ref. 4. Previous work on phonon focusing in sapphire includes three-dimensional theoretical plots of the phonon-flux intensity by Rösch and Weis (Ref. 7), a partial analysis of singularity structures by Taborek and Goodstein (Ref. 11), and use of optical methods for detecting ballistic phonons by Kaplyanskii *et al.* (Ref. 8).

We have obtained experimental phonon images for sapphire on samples of three different crystallographic orientations. Images for the first of these orientations, which has faces cut in the $[1\bar{1}02]$ direction, have been shown in Fig. 1, and the corresponding Monte Carlo image has been provided in Fig. 4(a). The "halo" seen in Fig. 1(a) is a surface-dependent feature that will be discussed in the next two sections. As can be seen in Fig. 1(b), when both surfaces of the sapphire are roughened this halo disappears. The remaining structures in the image are all due to bulk focusing.

The longitudinal sheet of the slowness surface for sapphire is entirely convex,²⁴ and hence there are no lines of parabolic points to give rise to focusing singularities. For completeness we show this sheet and the corresponding sheet of the wave surface in Figs. 2(c) and 3(c). However,

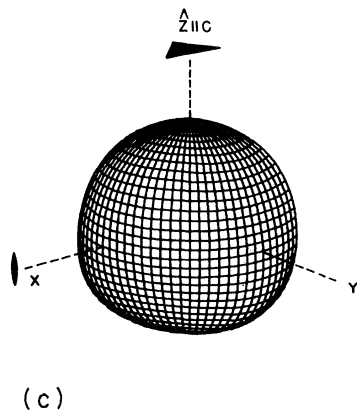
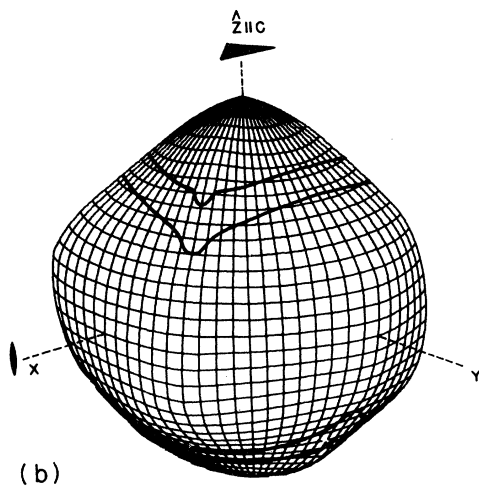
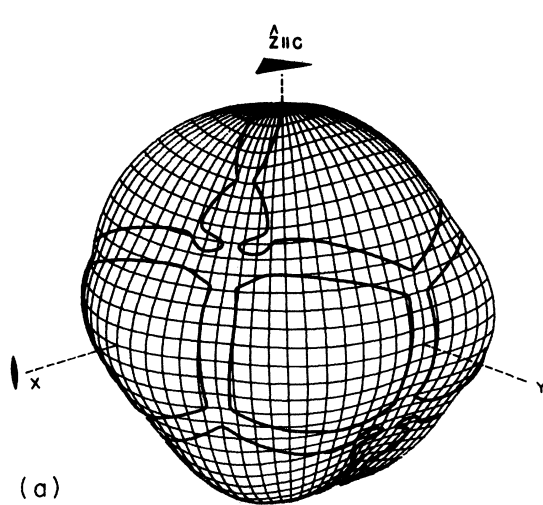


FIG. 2. Slowness surface for sapphire. It shows a grid of lines of constant θ_k and ϕ_k at 5-deg intervals in the range $-30^\circ \leq \phi_k \leq 120^\circ$ and $0^\circ \leq \theta_k \leq 180^\circ$. The lines of zero Gaussian curvature are shown as heavy lines. The Cartesian axes are oriented with respect to the standard hexagonal axes as follows: $X \parallel [11\bar{2}0]$, $Y \parallel [1\bar{1}00]$, $Z \parallel [0001]$. (a) ST sheet. (b) FT sheet. (c) L sheet.

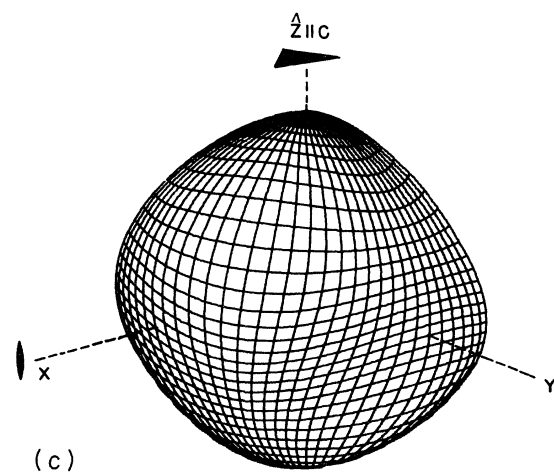
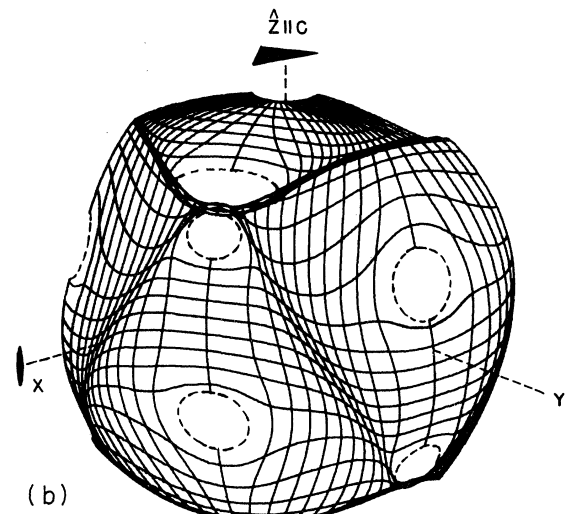
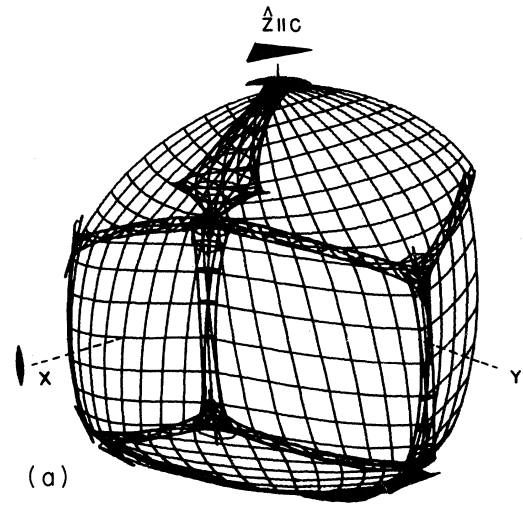


FIG. 3. Ray surface for sapphire. It has been constructed by mapping out the set of group velocities corresponding to the grid of slowness vectors in Fig. 2. The lines along which this surface is folded correspond to the lines of zero Gaussian curvature in Fig. 2. The dashed curves correspond to ellipses of conical refraction. (a) ST sheet. (b) FT sheet. (c) L sheet (reduced in size by a factor of 2).

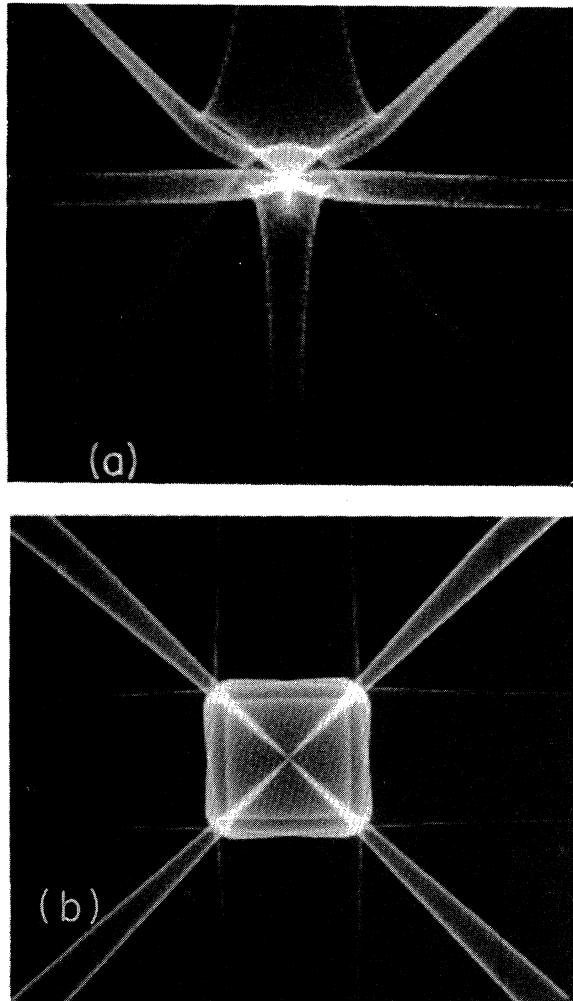


FIG. 4. (a) Monte Carlo calculation of the focusing pattern of sapphire for the same situation as in Fig. 1. This and later theoretical images are each composed of about 10^6 ray vectors. The computation requires about 20 min of CPU (central processing unit) time on a Digital Equipment Corporation computer VAX-11/750. (b) Monte Carlo image for germanium centered on the [100] direction. Interesting similarities can be seen between the images for sapphire and germanium.

the time gates for the experimental image were set to accept only slow transverse (ST) and fast transverse (FT) phonons emanating from the pulsed heat source. Likewise, the Monte Carlo image contains the flux pattern for ST and FT phonons but *not* for L phonons. Comparison between Figs. 1(b), 1(c), and 4 shows that there is good agreement between the experimental and theoretical images. The ST focusing pattern is composed of the necktie-like structure in the upper center, the horizontal "bar" across the center, and the vertical pedestal-like structure in the lower center of the image. The remaining structures, i.e., the narrow V -shaped band passing below the necktie-like structure to the upper corners and the two sloping ridges of high but nonsingular phonon intensity running from the center to the lower corners, are due to FT phonons. Comparison with the ray surfaces shown in

Figs. 3(a) and 3(b) reveals the correspondence between the caustics in the images and folds in the ray surface.

The two sloping FT ridges in the lower half of the image match the highly distorted regions of the ray surface where this surface is almost folded over on itself. In fact, it requires only modest changes in the elastic constants in order for the ray surface to develop pairs of folds along these distorted regions and in order for the sloping ridges in the phonon images to be transformed into genuine caustics. Similar well-defined ridges have been observed in experimental images for diamond¹² and quartz¹³ and also appear in theoretical images for numerous other substances. In general, they are precursors of genuine singularities, should the elastic constants be altered in a suitable way. In practice, this might be accomplished, for instance, by atomic substitution, externally applied stress, or variation of temperature. In the case of sapphire the changes in the elastic constants that affect this transformation bring the crystal closer to a situation of cubic symmetry and to an imaging pattern similar to that for germanium shown in Fig. 4(b). Comparison of Fig. 4(a) and 4(b) shows the interesting similarities between the images for these two crystals of different symmetry. In this particular case the precursors could therefore be regarded as relics of broken symmetry.

The second sapphire sample we have studied has surfaces normal to the crystallographic c axis. An experimental image obtained with this sample is shown in Fig. 5(a), and the Monte Carlo image for this view is shown in Fig. 5(b). These images display the required threefold rotational symmetry and three mirror symmetry planes. As with the previous orientation, only the effects of ST and FT phonons are shown. The various focusing structures identified for the previous orientation can be seen in this one also.

The additional features unaccounted for by bulk phonon focusing are the three faint X 's inside the lower portions of each necktie-like structure. This surface-dependent feature is more easily discernible in the enlargement shown in Fig. 6(a) and will be discussed in the next section.

The predicted pattern of caustics for this orientation is shown in Fig. 5(c). A theoretical image for the enlarged view is shown in Fig. 6(b). It has been calculated with the use of elastic constants measured by the cw resonance technique and extrapolated to 2 K.²⁵ Comparison between Figs. 6(a) and 6(b) shows the theoretical image to be qualitatively correct, but some minor quantitative differences remain. Figure 6(c) has been generated using elastic constants measured by the pulse-echo technique,²⁶ also extrapolated to 2 K. This second theoretical image is in better agreement with the experimental image even though the elastic constants were varied by only 1–5% from Fig. 6(b). This sensitivity of phonon images to the precise values of elastic constant ratios provides a useful check on the low-temperature values of these constants. In principle, one can determine these ratios from scratch using this technique.

An experimental image for our third sapphire sample is shown in Fig. 9(a). All the focusing structures observed for the other two orientations are present in this image as

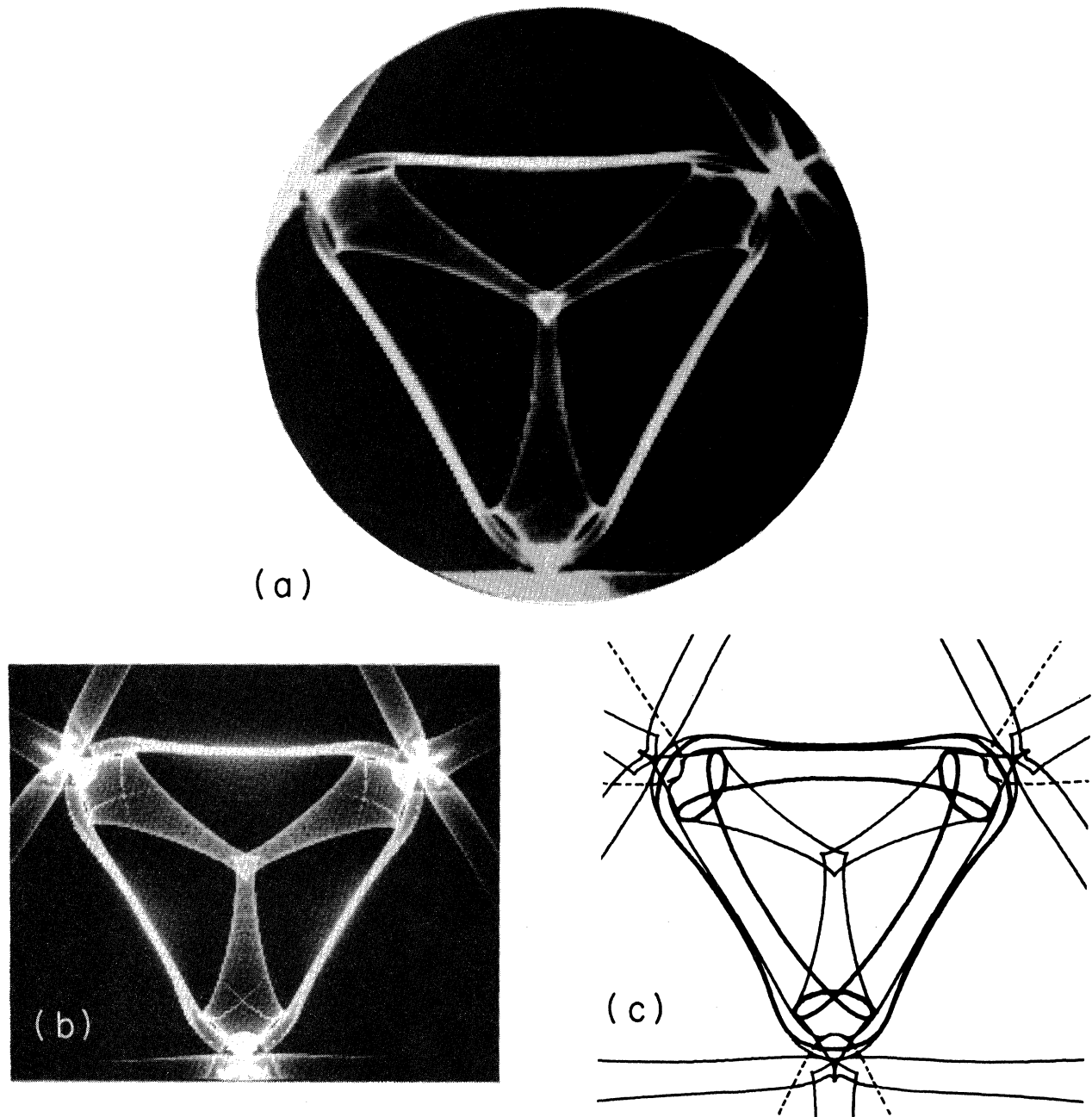


FIG. 5. (a) Experimental phonon image for sapphire with faces cut normal to the crystallographic c axis and polished. The image represents a radial scan of 58° . (b) Monte Carlo image for the same situation as in (a). The calculated critical-cone contours is denoted by the sequence of dots. The intensities of the dots are determined by the polarization condition discussed in the text. (c) Line drawings of the caustics and of the critical cone contours for the same orientation as (a) and (b).

well. This image contains additional information on critical-cone channeling and will be discussed further in the next section.

III. CRITICAL-CONE CHANNELING: EXPERIMENTAL AND GEOMETRICAL ASPECTS

As pointed out in the preceding section, there are structures in the ballistic phonon images of highly polished sapphire that cannot be explained on the basis of bulk focusing alone. These additional features correspond to a

sharply peaked angular distribution of phonon wave vectors. The phonon image shown in Fig. 1(a) contains a striking feature that is almost invisible in the accompanying phonon image in Fig. 1(b), which was obtained from a crystal of the same orientation but with surfaces roughened with a $1\text{-}\mu\text{m}$ diamond paste. The feature referred to is the large oval-shaped band or halo that is formed into four loops where it passes through pairs of ST caustics. Bulk-phonon focusing on its own does not predict the existence of this halo, although from the way

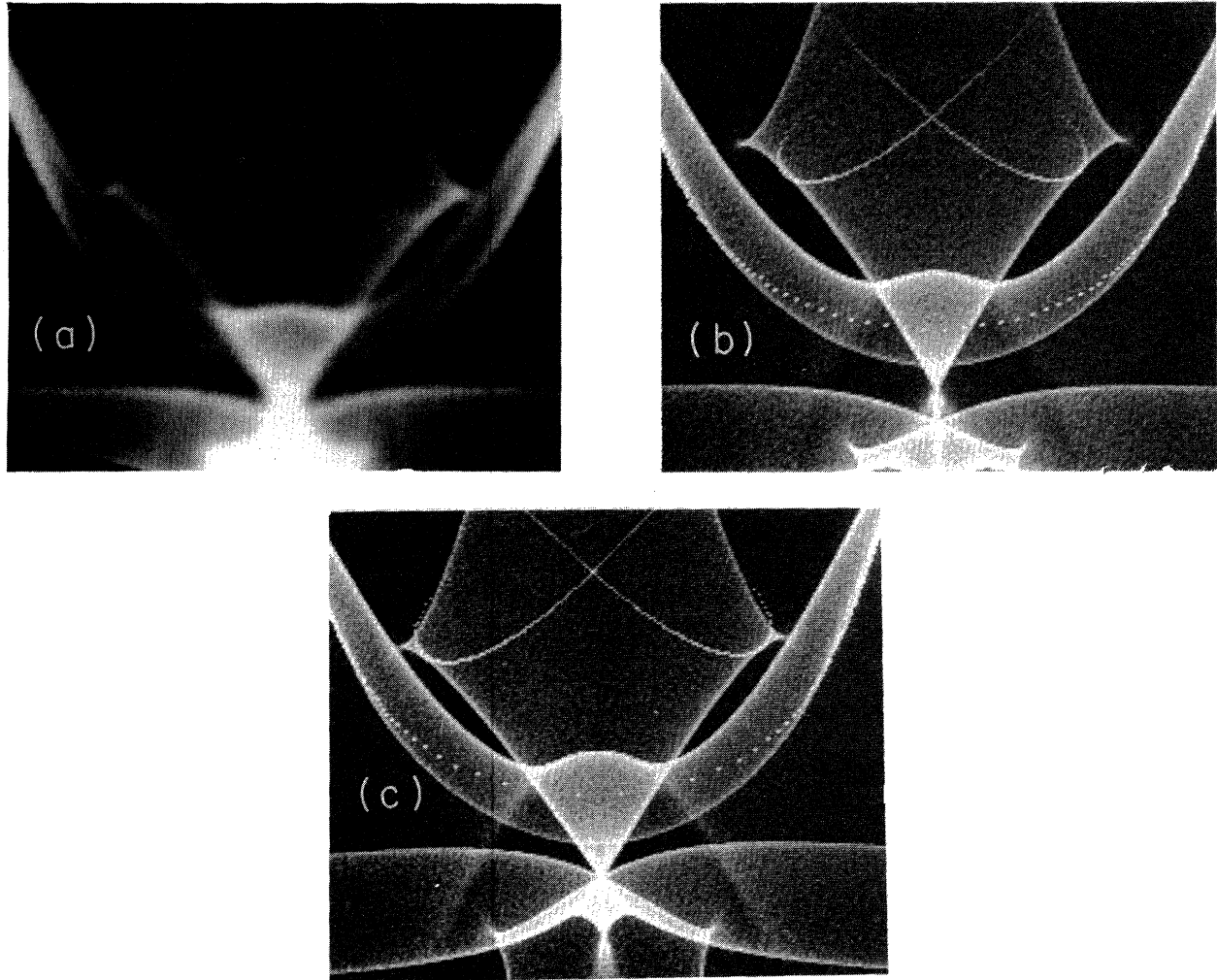


FIG. 6. (a) Enlargement of portion of the experimental phonon image of Fig. 5. (b) Theoretical image for the same situation as in (a), calculated with the elastic constant values $C_{11}=495.0$, $C_{12}=161.1$, $C_{13}=111.1$, $C_{14}=-22.2$, $C_{33}=499.9$, $C_{44}=147.7$, all in units of 10^{10} dyn/cm². These have been obtained by extrapolation to 2 K from values given in Ref. 25. (c) Theoretical image obtained using the elastic constant values $C_{11}=495.2$, $C_{12}=165.4$, $C_{13}=113.0$, $C_{14}=-23.2$, $C_{33}=493.2$, $C_{44}=148.8$, all in units of 10^{10} dyn/cm². These are low temperature values extrapolated from values given in Ref. 26.

the halo is deflected at the caustics it is evident that focusing does have an influence on its ultimate shape. In this section we discuss some simple geometrical ideas that allow the propagation directions and relative intensities of these wave-vector channeling structures to be predicted. There seems to be no evidence of wave-vector channeling features in the phonon images for sapphire obtained by Eichele *et al.*⁴ This probably stems from different surface conditions of the samples used in their and our experiments.

The sensitivity of the halo to surface condition and, as we shall see, also to surface orientation, shows that this new feature originates at the metal-crystal interface. Its existence implies that the phonon-transmission probability at this interface is strongly peaked along certain wave-vector directions. This wave-vector channeling effect is intrinsic to *both* interfaces. At the heater interface it results in a phonon distribution in the crystal that is rich in

\vec{k} 's along certain directions, whereas at the opposite interface it favors the transmission of phonons with certain selected \vec{k} 's from the crystal into the detector. Roughening one of the two faces of the crystal reduces the overall intensity of the channeling structure by about a factor of 2, while roughening both surfaces almost eliminates this feature, as Fig. 1(b) shows.

The roughening we have carried out has been on a scale ($\sim 1 \mu\text{m}$) that is large compared to the dominant phonon wavelengths, which are on the order of 100 \AA . One of the actions of the roughening is to present to different phonons crossing the interface surface segments that are tilted in a variety of directions with respect to the average surface normal. Thus any channeling taking place at the interface is smeared out in accordance with the distribution of surface-segment orientations. If this is a broad distribution, there is unlikely to be any clearly defined surface-derived structure surviving. Bron *et al.* (Ref. 15)

have suggested a similar mechanism hindering the piezoelectric generation of high-frequency phonons in quartz.

The characteristic that distinguishes the phonons in the halo of Fig. 1(a) from other phonons is that in the former all lie very close to the critical cone for mode conversion of ST to L waves at the crystal surface.¹⁹ In this phonon image there is also the faint presence of an analogous channeling structure for FT phonons.

The physical significance of the critical cone is portrayed in Fig. 7, which shows a schematic section of a slowness surface. For clarity only the L and one T sheet are shown, although critical cones do exist for both transverse sheets and are discussed below. In general, when a wave is incident on a crystal surface, it gives rise to three reflected waves.²⁰⁻²² All of these have the same frequency and are phase matched in the surface, i.e., they all have the same wave-vector component $\vec{k}_{||}$ or slowness component $\vec{S}_{||} = \vec{k}_{||}/\omega$ in that surface. When an incident T wave approaches at a small angle to the surface normal, i.e., \vec{S}_i lies *within* the critical cone, the three outgoing reflected waves are all bulk waves, having real components S_{\perp} of slowness normal to the surface. As the incident T wave approaches the T→L critical cone, the ray vector for the reflected L wave tilts over and ultimately becomes parallel to the surface. The slowness \vec{S}_l of the longitudinal wave does not, in general, at this stage lie in the surface, and, furthermore, the ray vectors \vec{V}_i of the incident T wave and \vec{V}_l of the reflected L wave do not, in general, lie in the sagittal plane, i.e., the plane containing the slownesses \vec{S}_i and \vec{S}_l and normal to the interface. When \vec{S}_i lies outside the critical cone, no bulk L wave is produced, but instead there is an evanescent L wave confined to the surface. The slowness vector for this L wave has component S_{\perp} , which is complex, the imaginary part resulting in the exponential extinction of the wave away from the surface.

The computational procedure we have followed has consisted in parametrizing the problem with respect to polar coordinates θ_s and ϕ_s of \vec{S} with respect to the normal to the surface. The azimuthal angle ϕ_s was set as a sequence of values spaced at regular intervals. For each value of ϕ_s , a root-finding technique was employed to locate the polar angle θ_s that rendered the ray velocity

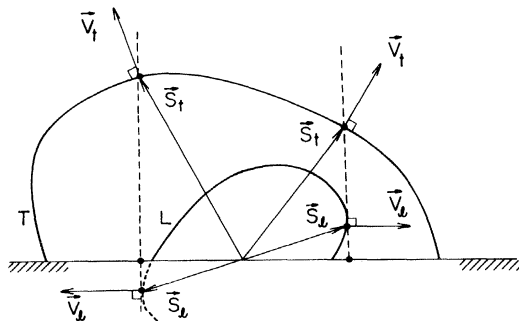


FIG. 7. Schematic view of section through a slowness surface showing the critical-cone condition.

$\vec{V}_l(\theta_s, \phi_s)$ parallel to the surface. The corresponding value of \vec{S}_l was obtained in the process.

The second stage of the calculation was to find the \vec{S}_l in this sagittal plane (same ϕ_s but different θ_s) that satisfied the phase-matching condition. The associated ray vector \vec{V}_l was then obtained and projected onto the opposite face of the crystal to determine the point of arrival of the associated portion of phonon flux. The totality of such \vec{S}_l vectors, for each of the experimental surface orientations of sapphire, turns out to lie fairly close to a circular cone of half-angle about 34° . [Indeed, if one were to assume elastic isotropy, this cone would be perfectly circular, and the half-angle would be $\theta_c = \arcsin(C_{44}/C_{11})^{1/2} \sim 33^\circ$.] The mapping to \vec{V} space, however, results in the much more complex curves shown in Figs. 1(c), 5(b), 5(c), 8(a), 8(b), and 9(b). This is because the cone intersects regions of curvature of different sign in the slowness surface, and hence the critical cone rays follow a contour on the ray surface that meets and is deflected by folds in that surface. A comparison between the experimental and calculated results shows that, as regards the location of the critical-cone channeling, agreement is extraordinarily good.

For the first orientation of sapphire, the FT channeling structure is very much fainter than the ST channeling structure. The reason for this can be attributed to the fact that the phonons comprising the FT structure for this particular orientation all happen to have polarization vectors directed very nearly perpendicular to the sagittal plane. Such phonons are expected to participate only weakly in mode conversion (in the case of an isotropic medium, waves of this type do not mode convert at all) and thus show little sign of critical-cone effects. For the other crystal orientation on which we report, this is not the case, and both ST and FT channeling structures are in evidence.

We demonstrate below that the simple expedient of projecting the polarization of the T phonon onto the sagittal plane and squaring is able to account fairly accurately for the relative intensities of the two critical-cone channeling structures. This weighting procedure has been used in calculating the critical-cone structures for the first orientation shown superposed on a theoretical phonon image in Fig. 8(a). The FT channeling structure is extremely faint compared to that of the ST structure, and the ST structure matches accurately the halo in the experimental image of Fig. 1(a). The calculated channeling structures for the *c*-axis orientation, taking account of the polarization dependence of the intensity, are shown in Fig. 5(b) superimposed on a theoretical phonon image for this orientation. In this case the FT channeling structure is actually much more intense than the ST structure, but the FT channeling structure lies entirely within the intense triangle-shaped band of FT caustics and is difficult to discern in both the experimental [Figs. 5(a) and 6(a)] and theoretical [Fig. 5(b)] images for this orientation. In order to reveal the shape of this structure unobscured by the FT caustics, it is shown again in Fig. 8(b), which contains a line drawing of the ST caustics with the FT caustics *omitted*. The ST channeling structure for this orientation only acquires appreciable intensity within the lower regions of the

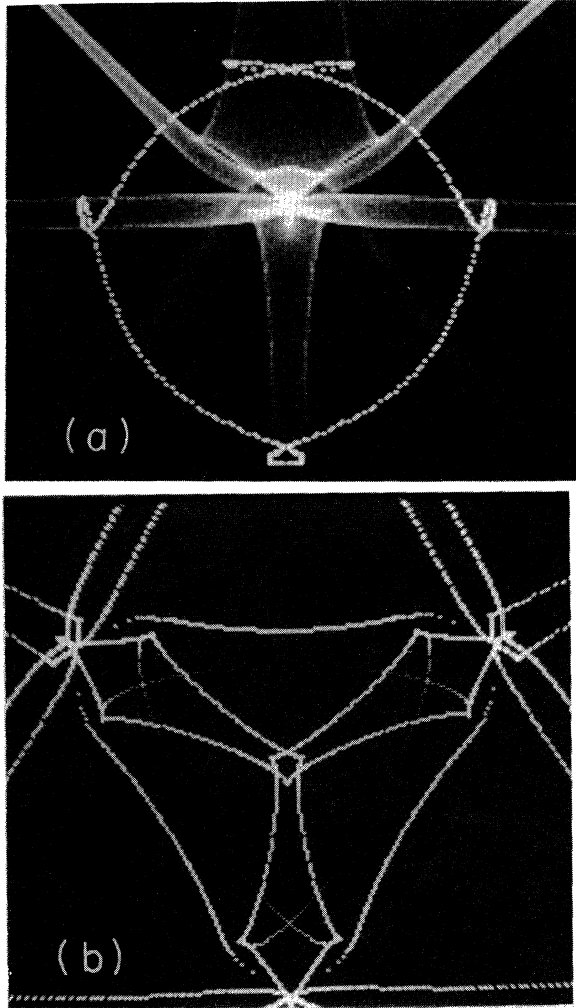


FIG. 8. (a) Monte Carlo image corresponding to Fig. 1. Critical-cone contours are shown by the sequence of dots, the intensity of which are determined by the polarization condition. (b) ST and FT critical-cone contours superposed on line drawing of ST caustics for the same situation as in Fig. 5.

necktie-like structures, where it takes on the appearance of a set of X 's. These accurately match the corresponding faint structures in the experimental images of Figs. 5(a) and 6(a).

A third crystal orientation with surface normal to the direction [$\theta=55^\circ$, $\phi=7^\circ$] shows a more even mixing of the two channeling structures. The experimental image is shown in Fig. 9(a), and the predicted channeling structures superimposed on a line drawing of the caustics are shown in Fig. 9(b). In this case, both FT and ST structures can be seen and there is reasonable agreement between theory and experiment as regards the location and intensity of these structures.

There are other types of modes conversion, with attendant cones of critical directions, that might also give rise to wave-vector channeling. The most obvious of these is ST \rightarrow FT conversion. The convoluted shape of the slowness surface for elastically anisotropic media, however, al-

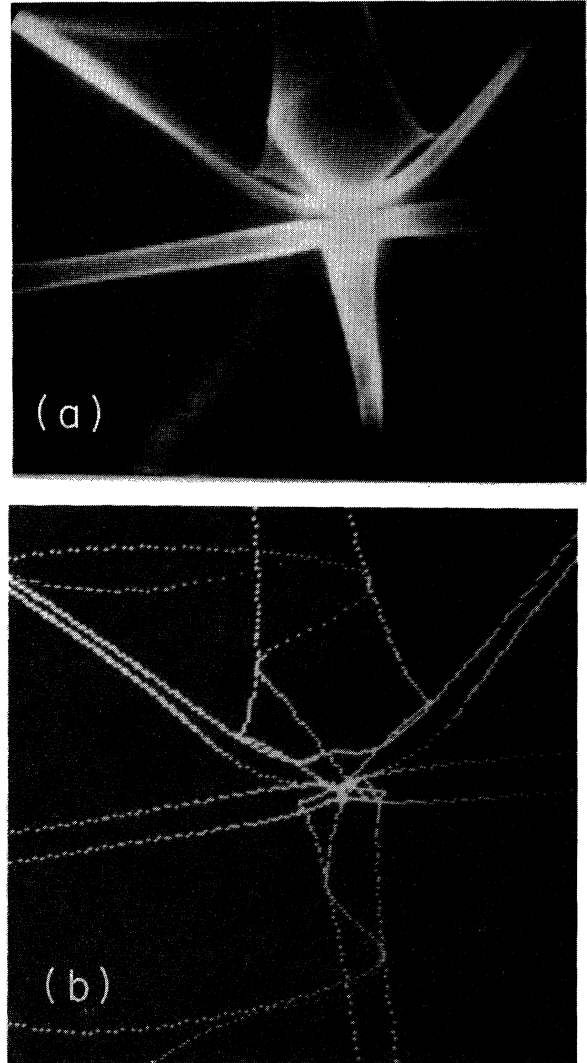


FIG. 9. (a) Experimental phonon image for sapphire with surfaces cut normal to the direction ($\theta=55^\circ$, $\phi=7^\circ$) and polished. (b) Line drawing of caustics and dotted critical-cone contours.

lows for other possibilities also. Depending on the orientation of the crystal surface with respect to concave and saddle-shaped regions of the slowness surface, mode conversion within a single transverse branch may occur. This phenomenon has been discussed in some detail by Musgrave²⁷ and Henneke.²⁸ When it does occur there are reentrant critical directions corresponding to the reemergence of a bulk wave from an evanescent wave as the angle of incidence is *increased*. For larger angles of incident there will be further critical directions where these bulk waves again give way to evanescent waves.

For sapphire these ST \rightarrow FT and other critical directions occur at fairly large angles to the surface normal, and so any channeling structures they might lead to lie out of the field of view of our experimental images. For this reason we have not investigated these in detail.

IV. CRITICAL-CONE CHANNELING: LOOSE BONDING MODEL OF AN INTERFACE

A. Loose bonding between two isotropic solids

The geometrical arguments of the preceding section enabled the shapes and relative intensities of the critical-cone structures to be predicted. They did not, however, explain the existence of these structures nor account for their finite width or their absolute intensity. In this section we present some preliminary results drawn from a physical model of two *isotropic* elastic solids loosely bonded to each other. This model is able to provide useful insights into the nature and origin of these observed structures and to identify conditions that are favorable for critical-cone channeling. The model is also able to account qualitatively for the intensity variation across the width of the channeling structures and to explain the comparative insensitivity of these structures to the type of metal heater film used.

The impetus for developing our model derives from information contained in Fig. 10. The inset in this figure shows graphically the conditions for mode conversion at a surface of a transverse wave that is polarized in the plane of incidence. When the incident angle θ is less than $\theta_c = \arcsin(V_t/V_l)$, there are both longitudinal and transverse reflected waves that meet the k_{\parallel} -conservation condition. When $\theta > \theta_c$, no longitudinal wave has a sufficiently large \vec{k} vector to satisfy k_{\parallel} conservation. The condition $k_{\parallel}^2 + k_{\perp}^2 = k_l^2 = \omega^2/V_l^2$ can, however, be satisfied by taking k_{\perp} to be imaginary, i.e., corresponding to an evanescent wave with displacement exponentially decreasing away from the surface. The dashed lines in the inset represent imaginary values of k_{\perp} . Figure 10 shows the squared am-

plitude $|\Gamma|^2$ of the reflected *L* wave for a unit-amplitude incident *T* wave. Three different conditions are depicted:

(a) The sapphire surface is traction-free, i.e., $\sigma_{ij}n_j = 0$, where σ_{ij} is the stress tensor and $\hat{n} = (n_i)$ is the normal to the surface.

(b) The sapphire surface is perfectly bonded to Cu. This requires continuity of traction force $\sigma_{ij}n_j$ and displacement field $\vec{u} = (u_i)$ across the interface.

(c) The sapphire surface is loosely bonded to Cu in the sense to be explained later in this section.

In each case the directions of the outgoing waves are governed by Snell's law, and the amplitudes are determined by the boundary conditions. As can be seen in Fig. 10, in case (a) there is a pronounced angular resonance in $|\Gamma|^2$ lying just beyond the critical angle $\theta_c = 33^\circ$. This resonance can be interpreted as the signature of a longitudinal pseudo-surface-wave.^{20,21,29}

It is worth reiterating here what the distinction is between a true surface wave and a pseudo-surface-wave. A true surface wave is a wave that satisfies the boundary conditions and that is composed of phase-matched *evanescent* partial waves *only* (i.e., no bulk partial waves). For a free surface this wave is known as a Rayleigh wave, and it consists of at most three partial waves (or two if the medium is isotropic), while for an interface between two different media it is known as a Stonely wave and is composed of at most six partial waves (or four if both media are isotropic). The Rayleigh wave is represented schematically by the small squares in the inset of Fig. 10. The sizes of these squares indicate the relative magnitudes of its partial waves. The velocity of a surface wave is less than that of any of the bulk waves in the relevant direction, and so it does not phase match to any bulk waves at the surface. A pseudo-surface-wave, on the other hand,

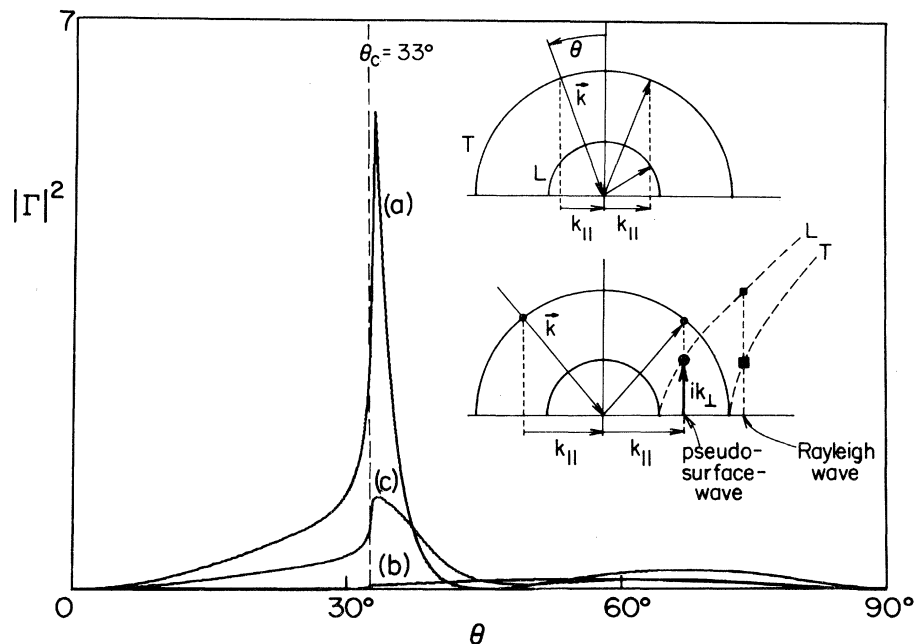


FIG. 10. Mode conversion from transverse to longitudinal waves at a sapphire/copper interface. The sapphire is taken to be isotropic with the sound velocities being $V_{cl} = 11.1$ km/sec and $V_{ct} = 6.04$ km/sec and density $\rho_c = 3.986$ g/cm³, and the corresponding values for Cu are $V_{ml} = 4.70$ km/sec, $V_{mt} = 2.26$ km/sec, and $\rho_m = 8.93$ g/cm³ (see Ref. 16). (a) no bonding, (b) perfect bonding, (c) loose bonding with coupling parameters $\alpha_{\parallel} = 1.0$, $\alpha_{\perp} = 1.1$.

has a velocity along the surface that is intermediate between the largest and smallest bulk velocities in its direction, and it is composed of both bulk and evanescent partial waves but with the *amplitudes of the evanescent wave component being much larger than the bulk wave component*. If the evanescent component is excited at the surface, this wave will propagate a considerable distance along the surface, only slowly radiating energy away from the surface into its bulk wave component (hence the name “leaky surface wave”). The pseudo-surface-wave is represented by the small circles in the inset of Fig. 10. The sizes of these circles indicate the relative magnitudes of the components.

The existence and location of the pseudo-surface-wave resonance in $|\Gamma|^2$ for the free sapphire surface strongly suggest the participation of this wave in the observed critical-cone channeling effect. Actually, case (a) is of formal interest only as there cannot be any phonon transmission across a free surface. On the other hand, we see in Fig. 10 that the pseudo-surface-wave resonance is almost totally suppressed when there is an ideal bond [case (b)] between the sapphire and Cu, or any other material of large acoustic impedance for that matter. The experimental situation would therefore appear to correspond to some sort of imperfect bonding as represented, say, by case (c) in Fig. 10. How might an intermediate or weak type of mechanical bonding therefore arise, and what is the simplest way of modeling it mathematically?

The granular metal films used in this investigation were produced by vapor deposition onto the crystal substrate, the surfaces of which had not been specially cleaned, although a rinse in ethanol and acetone before evaporation was usual. One might reasonably therefore expect the existence of a complex boundary layer between the metal and crystal that is composed of water vapor, possibly some hydrocarbons, oxides, highly disordered metal atoms, microvoids, etc.³⁰ It is difficult to gauge on *a priori* grounds what the precise acoustic characteristics of such a boundary layer are going to be. Indeed they will most probably vary depending on the prior history of the particular sapphire surface, how it has been handled, its temperature during evaporation of the metal film, and so on. The thickness of this boundary layer may well vary from point to point on the crystal surface, and the effective density and elastic constants can be expected to vary across the layer. Based in part on the weak acoustic coupling indicated by our experiments, we picture the general character of the boundary-layer material as loose and spongy rather than tightly coordinated, and thus the average density and elastic constants, and hence acoustic impedance, should be less than those of the adjacent bulk media. It is attractive to think that one might represent this type of boundary layer as a distributed compliance. If we ignore possible inertial effects associated with this compliance, then the traction forces $\sigma_{ij}(0_-)n_j$ and $\sigma_{ij}(0_+)n_j$ on the two sides of the interface are necessarily equal. In our model, we will allow a discontinuity in the displacement field at the interface, requiring only that the traction force be proportional to the relative displacement $\Delta u_i = u_i(0_+) - u_i(0_-)$ between the two media. The symmetry of the situation dictates that when the relative dis-

placement points along the interface, the traction force should be parallel to this displacement, while for a relative displacement normal to the interface the traction force should again be parallel to the displacement. The restoring force constants K_{\parallel} and K_{\perp} (per unit area of the interface) for these two directions will be treated as independent parameters of our model. When the relative displacement points in an arbitrary direction, its components normal and parallel to the interface are $(\Delta \vec{u} \cdot \hat{n})\hat{n}$ and $\Delta \vec{u} - (\Delta \vec{u} \cdot \hat{n})\hat{n}$, respectively. The traction force can be resolved in a similar way. Making use of the proposed proportionality between the forces and displacements, one obtains immediately that

$$\begin{aligned} \sigma_{ij}(0_-)n_j &= \sigma_{ij}(0_+)n_j \\ &= K_{\perp}(\Delta \vec{u} \cdot \hat{n})n_i + K_{\parallel}(\Delta u_i - (\Delta \vec{u} \cdot \hat{n})n_i) \\ &= [K_{\parallel}\delta_{ij} + (K_{\perp} - K_{\parallel})n_i n_j]\Delta u_j. \end{aligned} \quad (2)$$

In our model this set of six equations describing nonideal mechanical bonding between the two media replaces the normal boundary conditions for ideal bonding. In the weak-coupling limit, i.e., $K_{\parallel}, K_{\perp} \rightarrow 0$, Eq. (2) reverts to the boundary conditions for two independent traction-free surfaces, while the strong-coupling limit $K_{\parallel}, K_{\perp} \rightarrow \infty$ yields the conditions that apply to perfect bonding, i.e., continuity of displacement and traction force across the interface.

The appendix discusses some circumstances under which these boundary conditions would adequately represent the boundary layer. There is a higher cutoff frequency beyond which this approximation breaks down. Variation of K_{\parallel} and K_{\perp} along the interface is readily accommodated in this theory, providing that it takes place over distances on a scale that is large compared to the dominant phonon wavelength ($\sim 100 \text{ \AA}$ in our experiments). If this variation takes place more rapidly than this, local translational symmetry in the interface is lost and the \vec{k} -vector selection rules for phonon transitions break down. It is evident from the homogeneity of the experimental halos that the long-range variations are qualitatively rather small.

On purely dimensional grounds it is possible to express K_{\parallel} and K_{\perp} in the form

$$K_{\parallel} = \frac{\gamma_{\parallel}\mu'}{a}, \quad (3)$$

$$K_{\perp} = \frac{\gamma_{\perp}(\lambda' + 2\mu')}{a}. \quad (4)$$

where a is a lattice constant, λ' and μ' are conveniently chosen Lamé elastic constants³¹ that could, for instance, be taken to be those of sapphire (which we are here assuming isotropic), and γ_{\parallel} and γ_{\perp} are two dimensionless numbers. With the assumption that the effective elastic moduli of the boundary layer are small compared to those of the crystal and that the thickness of this layer is larger than the lattice spacing a , it follows that $\gamma_{\parallel} \approx \gamma_{\perp} \ll 1$. Also, we show in the Appendix that if the boundary-layer material satisfies the thermodynamic constraints on bulk

media (which seems plausible although it is not rigorously required), then $K_{\perp} > \frac{4}{3}K_{\parallel} > 0$.

B. Calculation of differential spectral emissivity

The adaptation of conventional acoustic mismatch theory to accommodate the boundary conditions postulated above is straightforward. Phonon transition probabilities at the interface are, as usual, given by the power transmission and reflection factors for incident acoustic waves.

To illustrate how the calculation of these factors proceeds, we consider an L wave of unit amplitude and frequency ω incident on the interface. The displacement of this wave is given by

$$\vec{u} = \hat{x} e^{i(\vec{k} \cdot \vec{r} - \omega t)}, \quad (5)$$

where \hat{x} is the polarization vector of the wave, \vec{r} is position, and t is time. This gives rise to a total of four outgoing waves as shown in Fig. 11, an L and an SV (transverse wave polarized in the plane of incidence) wave in each of the two media. The postulated boundary conditions preserve translational symmetry in the interface, and so the five partial waves are phase matched in the plane, i.e., their wave-vector components, $k_{\parallel} = k \sin\theta = (\omega/V)\sin\theta$, in the plane are all identical. Therefore the directions of these waves are related by Snell's law

$$\frac{\sin\theta_{cl}}{V_{cl}} = \frac{\sin\theta_{ct}}{V_{ct}} = \frac{\sin\theta_{ml}}{V_{ml}} = \frac{\sin\theta_{mt}}{V_{mt}}, \quad (6)$$

where the V 's are the different wave velocities, with the subscripts denoting the mode, L (l) or T (t), and the medium crystal (c) or metal (m). The stress fields accompanying these waves are derived from the stress-strain relationships

$$\sigma_{ij} = \mu \left[\frac{\partial u_i}{\partial r_j} + \frac{\partial u_j}{\partial r_i} \right] + \lambda \delta_{ij} \frac{\partial u_k}{\partial r_k} \quad (7)$$

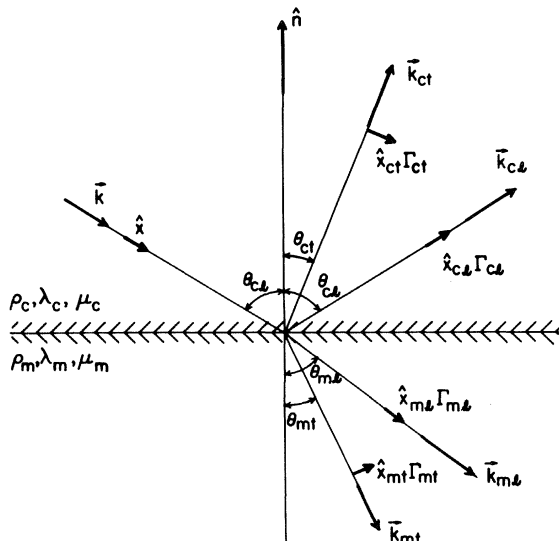


FIG. 11. Reflection and refraction of a longitudinal wave incident on a sapphire/metal interface.

for the two media. There are no displacements normal to the plane of incidence and consequently no traction forces in this direction. Two of the six boundary conditions are therefore automatically satisfied. The amplitudes $\Gamma_{cl}, \Gamma_{ct}, \Gamma_{ml}, \Gamma_{mt}$ of the four outgoing waves are determined by the requirement that the sum of the five partial waves should satisfy the remaining four boundary conditions. This yields the set of four inhomogeneous linear equations for the (complex) amplitudes:

$$\begin{pmatrix} A_{11} & A_{12} & A_{13} & A_{14} \\ A_{21} & A_{22} & A_{23} & A_{24} \\ A_{31} & A_{32} & A_{33} & A_{34} \\ A_{41} & A_{42} & A_{43} & A_{44} \end{pmatrix} \begin{pmatrix} \Gamma_{cl} \\ \Gamma_{ct} \\ \Gamma_{ml} \\ \Gamma_{mt} \end{pmatrix} = \begin{pmatrix} B_1 \\ B_2 \\ B_3 \\ B_4 \end{pmatrix}, \quad (8)$$

where the coefficients A_{ij} and B_j are functions of (i) the various angles, (ii) ratios of Lamé elastic constants $\lambda_c, \mu_c, \lambda_m$, and μ_m for the two media, and (iii) the dimensionless parameters

$$\alpha_{\parallel} = \frac{K_{\parallel} V_{ct}}{\mu_c \omega} \quad (9)$$

and

$$\alpha_{\perp} = \frac{K_{\perp} V_{cl}}{(\lambda_c + 2\mu_c)\omega}. \quad (10)$$

For example, typical coefficients are

$$A_{11} = \frac{\lambda_c + 2\mu_c}{\mu_c \sin\theta_{cl}} (i\alpha_{\parallel} \cos\theta_{cl} + 2 \sin^2\theta_{cl} - 1) \quad (11)$$

and

$$B_2 = -i\alpha_{\parallel} \frac{\sin\theta_{cl}}{\sin\theta_{ct}} - 2 \cos\theta_{cl}. \quad (12)$$

Equation (8) is solved numerically to obtain the amplitudes. A similar calculation yields the outgoing waves for an incident SV wave. To accommodate the multitude of scattering channels, we will employ the notation Γ_j^i for the amplitudes, $i = cl, ct, ml, mt$ specifying the incident wave and $j = cl, ct, ml, mt$ specifying the outgoing wave. The power factor of phonon-transition probability for mode i to mode j is given by

$$W_{i \rightarrow j} = \frac{\rho_j V_j |\Gamma_j^i|^2 \cos\theta_j}{\rho_i V_i \cos\theta_i}. \quad (13)$$

The transition probabilities are dependent on frequency through the coupling parameters α_{\parallel} and α_{\perp} . On setting $\alpha_{\parallel} \sim \alpha_{\perp} \sim 1$, we arrive at a characteristic scale of length

$$\Lambda_0 \sim \frac{2\pi a}{\gamma_{\parallel}} \sim \frac{2\pi a}{\gamma_{\perp}}, \quad (14)$$

against which the phonon wavelength Λ may be compared. For $\Lambda \gg \Lambda_0$, one has that $\alpha_{\parallel}, \alpha_{\perp} \gg 1$, and the interface is seen as nearly ideally bonded, while for $\Lambda \ll \Lambda_0$, one has that $\alpha_{\parallel}, \alpha_{\perp} \ll 1$; the effect is as if the two media were not joined at the interface and there is no transmission across the interface. The heat pulses used in our ex-

periment correspond to a temperature of about 10 K and hence to phonon wavelengths in the crystal on the order of 100 Å. We do not have any *a priori* method of predicting whether this is smaller or larger than Λ_0 . The experimental evidence, however, suggests that $\alpha_{||}$ and α_{\perp} are of order 1, and so the two lengths are comparable, and this can be used to obtain an estimate of $\gamma_{||}$ and γ_{\perp} . The intermediate case in Fig. 10 has been calculated by the above method and corresponds to $\alpha_{||}=1.0$, $\alpha_{\perp}=1.1$. (These values satisfy the bulk thermodynamic constraint $\alpha_{\perp}/\alpha_{||}=K_{\perp}V_{ct}/K_{||}V_{cl}>0.72$.)

In calculating the phonon radiation from the heater, we adopt the common assumption in heat-pulse analysis, namely that the heater film is in thermal equilibrium at a temperature T and that the crystal substrate is at a temperature $T_c \ll T$. Thus there is effectively a one-way flow of phonons from the heater film to the substrate. The spectral phonon flow for mode j from unit area of the radiating surface and per unit solid angle in direction θ with respect to the interface normal is readily shown to be

$$L_j(\omega, T, \theta) = f_j(\omega, T) \epsilon_j(\omega, \theta) \cos \theta, \quad (15)$$

where

$$f_j(\omega, T) = \frac{\bar{n} \hbar \omega^3}{8\pi^3 V_j^2} \quad (16)$$

is the spectral power flow when both metal and crystal are at the same temperature T ,

$$\bar{n} = \frac{1}{\exp(\hbar\omega/k_B T) - 1} \quad (17)$$

is the phonon occupation number, \hbar is Planck's constant divided by 2π , k_B is Boltzmann's constant, and $\epsilon_j(\omega, \theta)$ is the differential spectral emissivity of the interface for radiation into mode j . For an ideal "black-body radiator" ϵ would be unity, the largest value it can attain on thermodynamic grounds.³² The $\cos\theta$ term expresses Lambert's law for the radiating surface. Emissivities can be written as simple linear combinations of phonon transmission probabilities or by making use of the principle of detailed balance in terms of reflection probabilities. Thus, for instance, the emissivity for SV phonons into the crystal is

$$\epsilon_{ct}(\omega, \theta) = \begin{cases} 1 - W_{cl \rightarrow ct} - W_{ct \rightarrow ct}, & \theta \leq \theta_c \\ 1 - W_{ct \rightarrow ct}, & \theta > \theta_c \end{cases} \quad (18)$$

where $W_{i \rightarrow j}$ is expressed as a function of ω and $\theta \equiv \theta_{ct}$, while for L phonons into the crystal the emissivity is

$$\epsilon_{cl}(\omega, \theta) = 1 - W_{cl \rightarrow cl} - W_{ct \rightarrow cl}, \quad (19)$$

where in this case $W_{i \rightarrow j}$ is expressed in terms of ω and $\theta \equiv \theta_{cl}$.

Figure 12 shows a number of plots of ϵ_{ct} vs θ for the Cu/sapphire combination and for a number of different values of $\alpha_{||}$ and α_{\perp} . The most striking feature about these curves is that when $\alpha_{||}$ and α_{\perp} are of order 1 or smaller (i.e., $\Lambda \lesssim \Lambda_0$), there is a pronounced peak lying just beyond θ_c . This peak is associated with the pseudo-surface-wave mentioned earlier. As $\alpha_{||}$ and α_{\perp} are reduced progressively further below 1, the overall emissivity de-

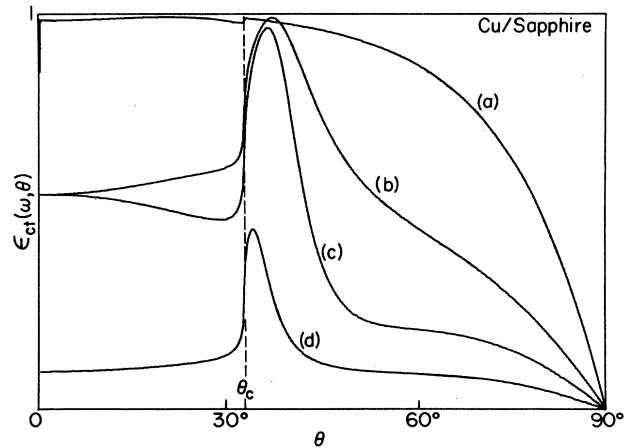


FIG. 12. Differential spectral emissivity $\epsilon_{ct}(\omega, \theta)$ for copper into sapphire (assumed isotropic) for a number of different values of the coupling parameters: (a) $\alpha_{||}=10$, $\alpha_{\perp}=10$, (b) $\alpha_{||}=1$, $\alpha_{\perp}=1$, (c) $\alpha_{||}=1$, $\alpha_{\perp}=0.5$, (d) $\alpha_{||}=0.3$, $\alpha_{\perp}=0.3$.

creases steadily. Eventually, the width of the peak approaches a constant value independent of $\alpha_{||}/\alpha_{\perp}$, and the ratio of the height of the peak to the background approaches a value that is a function of $\alpha_{||}/\alpha_{\perp}$.

When $\alpha_{||}, \alpha_{\perp} \gg 1$ (i.e., $\Lambda \gg \Lambda_0$) there is a barely perceptible feature in $\epsilon_{ct}(\omega, \theta)$ at θ_c , and the peak is broadened beyond recognition. This latter case corresponds to a sapphire surface that, in effect, is perfectly bonded to a medium of high acoustic impedance, and the freedom that is required for the pseudo-surface-wave to exist in the sapphire no longer exists.

Figure 13 shows a similar set of plots for the combination Al/sapphire. Again, for $\alpha_{||}, \alpha_{\perp} \leq 1$ the resonance near θ_c is the dominant feature, and its dependence on $\alpha_{||}$ and α_{\perp} is the same as that for the Cu/sapphire combination.

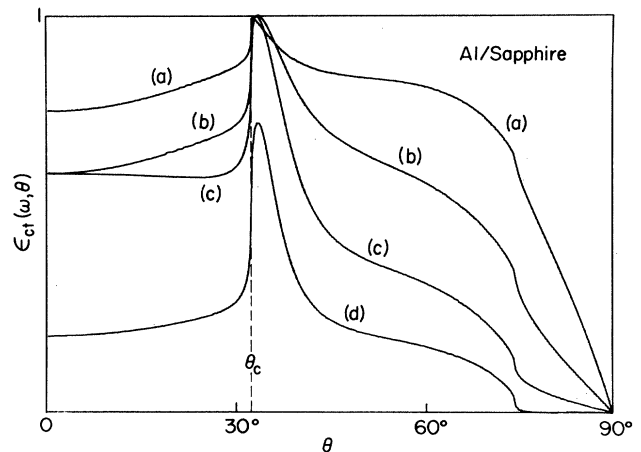


FIG. 13. Differential spectral emissivity $\epsilon_{ct}(\omega, \theta)$ for aluminum into sapphire for a number of values of the coupling parameters: (a) $\alpha_{||}=10$, $\alpha_{\perp}=10$, (b) $\alpha_{||}=1$, $\alpha_{\perp}=1$, (c) $\alpha_{||}=1$, $\alpha_{\perp}=0.5$, (d) $\alpha_{||}=0.3$, $\alpha_{\perp}=0.3$. The velocities for Al have been taken as $V_{m1}=6.26$ km/sec and $V_{m2}=3.08$ km/sec, and density $\rho_m=2.70$ g/cm³ (see Ref. 16).

Moreover, the peak has essentially the same shape as that in the Cu/sapphire case, i.e., it is skewed, rising more steeply on the inside (small θ). It is clear, therefore, that this resonance is a feature that is intrinsic to the sapphire surface and is not strongly influenced by the adjacent metal film and the coupling constants, providing the coupling is "weak." Interestingly, we note that for $\alpha_{||}, \alpha_{\perp} \gg 1$, in the case of Al/sapphire, the resonance is still present although reduced in intensity compared to that of the background. The reason for this is that the acoustic impedance of Al is appreciably smaller than that of sapphire, and so the sapphire surface is not as constrained as when it is bonded to Cu. In fact, reducing the acoustic impedance of the metal film has almost the same effect in enhancing the relative intensity of the resonance as reducing the magnitude of the coupling parameters. In the case of a second medium of very low acoustic impedance compared to that of sapphire, the resonance is fully developed even for perfect coupling.

This effect is reminiscent of the phenomenon of critical-angle reflectivity that is used as a diagnostic tool for examining surfaces³³ and that has also been invoked in connection with the Kapitza resistance between solids and liquid helium.³⁴ In this case a compressional wave in a liquid is used to excite a Rayleigh wave in a solid surface, and a resonant dip appears in the variation of the reflectivity with direction. In critical-angle reflectivity, the acoustic impedance of the liquid is, in general, considerably smaller than that of the solid, and so the Rayleigh resonance is only slightly broadened, and the need to consider modified boundary conditions (as done here) appears not to have arisen. An important distinction between the two effects is that the Rayleigh wave, unlike the pseudo-surface-wave, does not phase match onto any bulk acoustic wave in the solid, and so some form of attenuation mechanism, such as scattering by dislocations or free electrons, must be invoked for removing energy from the Rayleigh wave. For the pseudo-surface-wave, energy is naturally removed from the surface by the bulk-wave component. Bulk attenuation is not required and, in fact, would tend to mask the observed effect since it would limit the transmission of the ballistic T phonons through the crystal. Certainly there can be appreciable attenuation in the metal film. Our calculations, however, show that attenuation there has very little influence on critical-cone channeling.

C. Differential emissivity

Because $\epsilon_{ct}(\omega, \theta)$ is a function of the frequency ω , the spectrum of phonons entering the crystal does not correspond to the Planck distribution of phonons striking the interface from the metal side. As we have seen, the transmission probability and hence the emissivity decrease with increasing frequency (i.e., decreasing $\alpha_{||}$ and α_{\perp}), and hence higher-frequency phonons will be comparatively scarce in the transmitted flux. This effect will be less so in channeling directions where initially the emissivity does not decrease as rapidly as ω is increased. A quantity that is of more direct physical relevance in this context than the spectral phonon power flow is the integrated power

flow $L_j(T, \theta)$, which is obtained by integrating Eq. (15) with respect to ω :

$$L_j(T, \theta) = \int_0^{\infty} f_j(\omega, T) \epsilon_j(\omega, \theta) \cos \theta d\omega \\ = g_j(T) \tilde{\epsilon}_j(T, \theta) \cos \theta, \quad (20)$$

where

$$g_j(T) = \frac{\pi k_B^4 T^4}{120 \hbar^3 V_j^2}, \quad (21)$$

and

$$\tilde{\epsilon}_j(T, \theta) = \frac{15}{\pi^4} \int_0^{\infty} \frac{x^3}{e^x - 1} \epsilon_j \left[\frac{k_B T}{\hbar} x, \theta \right] dx \quad (22)$$

is the differential emissivity of the interface.

Figure 14 shows $\tilde{\epsilon}_{ct}(T, \theta)$ for the Cu/sapphire interface for several values of

$$\eta_{||} = \frac{\alpha_{||}}{k_B T / \hbar \omega} = \frac{\gamma_{||} T_t}{\pi T} \quad (23)$$

and

$$\eta_{\perp} = \frac{\alpha_{\perp}}{k_B T / \hbar \omega} = \frac{\gamma_{\perp} T_l}{\pi T}, \quad (24)$$

where the two quantities

$$T_t = \frac{\hbar}{k_B} V_{ct} \frac{\pi}{a} \quad (25)$$

and

$$T_l = \frac{\hbar}{k_B} V_{cl} \frac{\pi}{a}. \quad (26)$$

are temperatures on the order of the Debye temperature T_D . As can be seen in Fig. 14, when $\eta_{||}$ and η_{\perp} are of order 1 or smaller (i.e., T is sufficiently high so that the dominant phonons experience reasonably loosely bonded conditions at the interface), as with $\epsilon_{ct}(\omega, \theta)$, a peak occurs just beyond θ_c . The averaging process carried out by the integral in Eq. (22) has, however, resulted in the broadening of this peak.

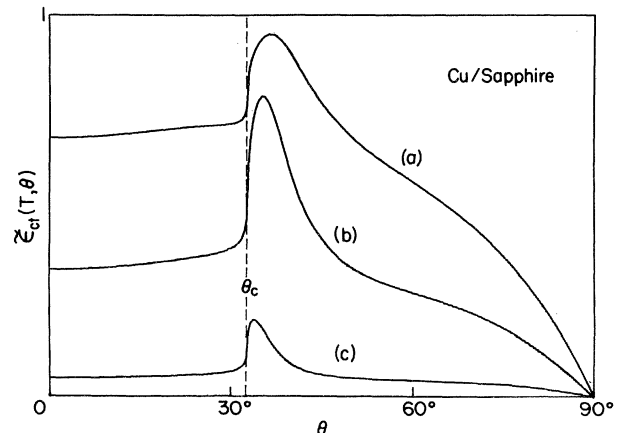


FIG. 14. Differential emissivity $\tilde{\epsilon}_{ct}(T, \theta)$ for copper into sapphire for (a) $\eta_{||} = \eta_{\perp} = 5$, (b) $\eta_{||} = \eta_{\perp} = 2$, (c) $\eta_{||} = \eta_{\perp} = 0.5$.

Figure 15 shows a plot of experimental detector signal as the propagation angle θ is scanned across the critical-cone halo in Fig. 1(a), i.e., a line scan as depicted in Fig. 1(c). The halo intensity corresponds to about a factor of 2 increase in flux intensity over the background. A comparison of Figs. 14 and 15 shows that there is a reasonable similarity between the shapes of the experimental and theoretical peaks when $\eta_{||} \approx \eta_{\perp} \sim 1$ to within about a factor of ~ 2 . For a reasonable value of $T_D/T \sim 100$ this means that $\gamma_{||} \sim \gamma_{\perp} \sim \frac{1}{30}$, i.e., $K_{\perp} \sim (\lambda + 2\mu)/30a$, $K_{||} \sim \mu/30a$. In simple terms this implies that the boundary layer has a compliance about 30 times that between two adjacent atomic layers of sapphire. This would be consistent, say, with a boundary layer of 10 atomic spacings and an effective moduli about one-third of those of sapphire. Thus our results indicate that the bonding between sapphire and metal in our experiments is far from perfect. Thermal phonons allow us to probe this imperfect bond on a microscopic scale. In contrast, owing to the frequency dependence of the coupling parameters $\alpha_{||}$ and α_{\perp} , the transmission of acoustic waves with GHz or less frequency is not significantly affected by this imperfect bonding.

D. Channeling at the detector interface

A similar channeling process takes place at the detector interface. At this interface, the spectral absorptivity $\phi_{ct}(\omega, \theta)$ for SV phonons is equal to $1 - (\text{spectral reflectivity})$, i.e.,

$$\phi_{ct}(\omega, \theta) = \begin{cases} 1 - W_{ct \rightarrow cl} - W_{ct \rightarrow ct}, & \theta \leq \theta_c \\ 1 - W_{ct \rightarrow cl}, & \theta \geq \theta_c \end{cases} \quad (27)$$

and there is a similar absorptivity

$$\phi_{cl}(\omega, \theta) = 1 - W_{cl \rightarrow cl} - W_{cl \rightarrow ct} \quad (28)$$

for L phonons. In Eq. (27) θ refers to the direction of the T phonons, while in Eq. (28) it refers to the direction of the L phonons. Comparison between Eqs. (18), (19), (27), and (28) reveals the close relationship

$$\begin{aligned} \epsilon_{ct}(\omega, \theta_{cl}) + \epsilon_{ct}(\omega, \theta_{ct}) &= \phi_{cl}(\omega, \theta_{cl}) + \phi_{ct}(\omega, \theta_{cl}), & \theta_{ct} \leq \theta_c \\ \epsilon_{ct}(\omega, \theta_{ct}) &= \phi_{ct}(\omega, \theta_{ct}), & \theta_{ct} > \theta_c \end{aligned} \quad (29)$$

connecting the emissivities and absorptivities. In the above equation subscripts ct or cl are attached to θ to distinguish between directions for T and L phonons. The sharp peak lying just beyond θ_c shows up in exactly the same form in the SV absorptivity and emissivity.

For an incident flux of phonons having a Planck-type distribution of frequencies a differential absorptivity $\tilde{\phi}_{ct}(T, \theta)$ can be generated by integration over ω and, just as with $\tilde{\epsilon}_{ct}(T, \theta)$, the peak near θ_c survives for sufficiently high Planck temperature.

Thus the critical-cone channeling process is shared (not necessarily in equal proportions) by the radiator and detector interfaces. It is straightforward to calculate the net spectral transfer rate of phonons from the heater through the crystal into the detector. With the assumption of no phonon scattering in the bulk of the crystal, this rate will be proportional to $f_j(\omega, T)\epsilon_j(\omega, \theta) \times \phi_j(\omega, \theta)\cos^2\theta$. By integrating over frequency, one obtains the total transfer rate. The main qualitative change is a slight sharpening of the peak.

Thus we see qualitatively similar results emerging for a variety of different approaches. The main point is that when the sapphire surface is relatively unimpeded in its movement by its bonding to an adjoining medium, a pseudo-surface-wave can exist at that surface, and this

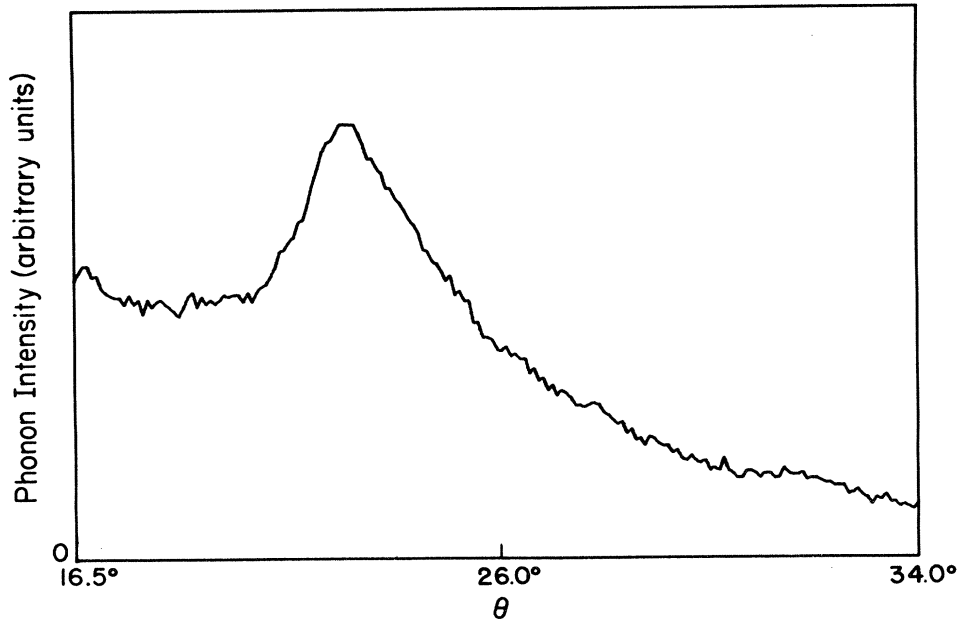


FIG. 15. A line scan taken across the halo in Fig. 1(a), showing phonon intensity variation with direction. The location of the scan line with respect to the phonon caustics is shown in Fig. 1(c). Owing to focusing the real-space position of the halo is shifted from $\sim 33^\circ$ to $\sim 22^\circ$.

wave plays an important role in the transfer of thermal phonons across that interface. The phonons that are assisted by this process are selectively channeled into directions close to the critical cone. There may possibly be other formulations of the boundary conditions, apart from the type we have proposed in this paper, that are able to account for the observed channeling intensity, but they will almost certainly embody, in some form, the idea of "weak" coupling.

Our findings here contain important implications for the theory of thermal boundary resistance and phonon-reflection effects at interfaces. The decrease in emissivity caused by loose bonding implies an increase in thermal boundary resistance. This is consistent with the general observation that measured thermal boundary resistances for solid-solid interfaces are often somewhat larger (by up to a factor of 2 or so) than their calculated values, and that the differences tend to increase with increasing temperature (see, e.g., Ref. 35).

The decrease in the emissivity as the effective coupling strength is decreased also goes hand in hand with an increase in the reflectivity coefficients, as examination of Eq. (29) shows. This may well explain the anomalously large phonon reflection coefficients reported by Marx and Eisenmenger for silicon-metal interfaces (see Ref. 14). Actually, these authors claim that their Si crystals are geometrically rough and that the phonon scattering at the interfaces is largely diffusive. Roughness, however, does not explain the large reflectivity. When two media of very similar acoustic properties are in intimate contact, the reflectivity of the interface is small, regardless of whether the interfaces is smooth or rough. Large reflectivity in this situation implies that there is a "soft" boundary layer or loose bonding between the adjoining media of the type we have discussed here.

V. CONCLUSIONS

We have shown in this paper that phonon imaging is a useful source of information on both bulk and surface influences on ballistic phonon propagation in crystals. The sapphire crystals we have studied display three types of well-defined structures in their phonon images. The first two are focusing singularities and near-singularities, respectively, which come about as a result of bulk elastic anisotropy.

The third type of structure we report on originates at the interfaces between the crystal and the heater and detector metal films. It corresponds to a highly nonuniform distribution of phonon wave-vector directions that is maximized near to the critical cone for mode conversion between T and L waves at the crystal surface. The presence of this type of structure demonstrates that on the scale of the dominant phonon wavelength ~ 100 Å the polished surfaces of our sapphire crystals are at least partially flat. The existence of these wave-vector channeling structures is related to the generation of longitudinal pseudo-surface-waves at the crystal surface, and this requires that the surface is only slightly constrained by the metal film to which it is bonded. We have proposed a model employing boundary conditions that takes account

of loose bonding between crystal and metal film. This model is able to explain the presence of the channeling structures and qualitatively account for their intensity variation.

The use of this model in conjunction with our experimental results has provided for the first time a quantitative measure of the bonding between sapphire and metal films. The bonding is found to be quite weak on an atomic scale, giving rise to a large critical-cone channeling effect, but still consistent with the high transmission of low-frequency waves across such an interface. These results provide a model for understanding the anomalous transmission and reflection at crystal-metal interfaces as reported in previous conductance and heat-pulse experiments.

ACKNOWLEDGMENTS

The phonon-focusing calculations employed in this paper made use of general computer programs developed by Northrop.²³ We also thank G. A. Northrop for discussions and experimental assistance in the initial stages of this work. We acknowledge useful discussions with A. C. Anderson. The research was supported by the National Science Foundation under the Materials Research Laboratories Program Grant No. DMR-80-20250. One of us (A.G.E.) would like to thank the University of the Witwatersrand and the Council for Scientific and Industrial Research for financial support.

APPENDIX: DERIVATION OF EFFECTIVE BOUNDARY CONDITIONS

Recently there have been a number of papers demonstrating how the problems of rough surfaces³⁶ or surface overlayers³⁷ can be advantageously recast in terms of equivalent boundary conditions. In the process the crucial parameters for the scattering of acoustic waves or phonons are identified and unimportant features and details are eliminated. In general, a characteristic scale of length appears in these theories, and the equivalent boundary conditions only apply for wavelengths greater than this size. In this appendix we describe how the boundary conditions used in Sec. IV can be derived from a boundary layer of a fairly general nature.

Figure 16 shows a layer of isotropic material of thickness h , density ρ , and Lamé elastic constants λ and μ sandwiched between two semi-infinite isotropic elastic media having corresponding material constants ρ_1, λ_1, μ_1 and ρ_2, λ_2, μ_2 . In the direction normal to the interface, distances are given in terms of x'_3 inside the layer ($0 \leq x'_3 \leq h$) and x_3 in the adjacent media. The two interfaces conform to normal boundary conditions, i.e., continuity of displacement and traction force.

Let us consider a plane SH wave (a transverse wave polarized normal to the plane of incidence, i.e., in the x_2 direction) of frequency ω , incident on this layer from below giving rise to the various reflected and refracted waves as shown. Inside the layer the displacement field is given by

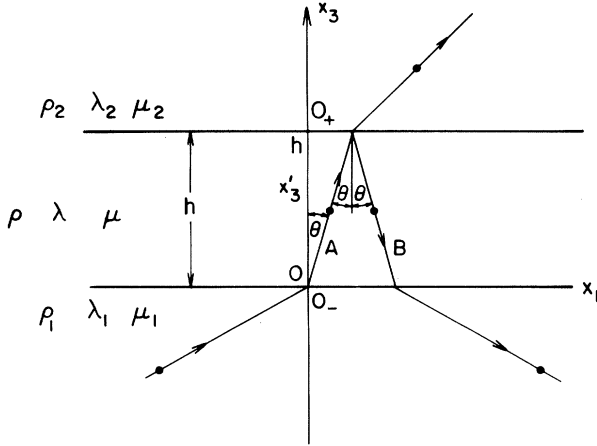


FIG. 16. Reflection and refraction of an SV wave at a thin film of material sandwiched between two other media.

$$u_2 = A \exp\{i[k(x_1 \sin\theta + x'_3 \cos\theta) - \omega t]\} + B \exp\{i[k(x_1 \sin\theta - x'_3 \cos\theta) - \omega t]\},$$

$$u_1 = u_3 = 0, \quad (\text{A1})$$

where $k = \omega/V_t = \omega(\rho/\mu)^{1/2}$ and A and B are the amplitudes of the two waves. It follows that the traction-force components of the stress within the layer are

$$\sigma_{13} = \sigma_{33} = 0, \quad (\text{A2})$$

$$\sigma_{23} = \mu \left[\frac{\partial u_3}{\partial x_2} + \frac{\partial u_2}{\partial x'_3} \right]$$

$$= i\mu k (\cos\theta) A \exp\{i[k(x_1 \sin\theta + x'_3 \cos\theta) - \omega t]\} - i\mu k (\cos\theta) B \exp\{i[k(x_1 \sin\theta - x'_3 \cos\theta) - \omega t]\}.$$

We may use Eq. (A1) to express A and B in terms of the displacements at $(x'_3 = 0) \sim (x_3 = 0_-)$ and $(x'_3 = h) \sim (x_3 = 0_+)$ and then substitute into Eq. (A2) to obtain the stresses $\sigma_{23}(x_3 = 0_-)$ and $\sigma_{23}(x_3 = 0_+)$ at the upper and lower surfaces. The result can be written in the form

$$\sigma_{23}(0_-) = f(\vec{k})[u_2(0_+) - u_2(0_-)] + g(\vec{k})[u_2(0_+) + u_2(0_-)], \quad (\text{A3})$$

$$\sigma_{ij}(0_+)n_j \approx \sigma_{ij}(0_-)n_j \approx [K_{||}\delta_{ij} + (K_{\perp} - K_{||})n_i n_j][u_j(0_+) - u_j(0_-)], \quad kh \ll 1. \quad (\text{A12})$$

The generalization to a finite or infinite number of layers is straightforward and simply requires that admittances be summed, i.e.,

$$(K_{||})_{\text{eff}}^{-1} = \sum_i (K_{||}^i)^{-1} \quad (\text{A13})$$

and

$$(K_{\perp})_{\text{eff}}^{-1} = \sum_i (K_{\perp}^i)^{-1}, \quad (\text{A14})$$

$$\sigma_{23}(0_+) = f(\vec{k})[u_2(0_+) - u_2(0_-)] - g(\vec{k})[u_2(0_+) + u_2(0_-)], \quad (\text{A4})$$

where

$$f(\vec{k}) = \frac{\mu k (\cos\theta) \cos[(kh \cos\theta)/2]}{2 \sin[(kh \cos\theta)/2]} \quad (\text{A5})$$

and

$$g(\vec{k}) = \frac{\mu k (\cos\theta) \sin[(kh \cos\theta)/2]}{2 \cos[(kh \cos\theta)/2]}, \quad (\text{A6})$$

are wave-vector-dependent coupling coefficients. In the long-wavelength limit ($kh \ll 1$), expanding these coefficients leads to the much simpler result:

$$\sigma_{23}(0_-) = K_{||}[u_2(0_+) - u_2(0_-)] + O(k^2 h), \quad (\text{A7})$$

$$\sigma_{23}(0_+) = K_{||}[u_2(0_+) - u_2(0_-)] + O(k^2 h),$$

which involves a single wave-vector-independent coupling constant

$$K_{||} = \mu/h. \quad (\text{A8})$$

In a similar way we can treat an incident L or SV wave. Owing to mode conversion between L and SV there are now four waves in the layer and therefore four amplitudes to consider. These amplitudes can, as above, be expressed in terms of displacements at the boundaries, and analogous equations to (A3) and (A4) derived. On expanding the coupling coefficients one finds, to leading order, that

$$\sigma_{13}(0_-) \approx \sigma_{13}(0_+) \approx K_{||}[u_1(0_+) - u_1(0_-)], \quad kh \ll 1 \quad (\text{A9})$$

and

$$\sigma_{33}(0_-) \approx \sigma_{33}(0_+) \approx K_{\perp}[u_3(0_+) - u_3(0_-)], \quad kh \ll 1 \quad (\text{A10})$$

where

$$K_{\perp} = \frac{\lambda + 2\mu}{h} \quad (\text{A11})$$

is a second coupling constant. Equations (A7), (A9), and (A10) are conveniently summarized for a plane interface of arbitrary normal $\hat{n} = (n_i)$ by the single tensor equation

where $K_{||}^i$ and K_{\perp}^i are the coupling constants for the individual layers and $(K_{||})_{\text{eff}}$ and $(K_{\perp})_{\text{eff}}$ are the effective coupling constants for the composite layer. The overall limitation on the validity of this approximation is that

$$\sum_i k_i h_i \ll 1. \quad (\text{A15})$$

The normal thermodynamic constraints on bulk materials (that the bulk and rigidity moduli should be positive) require that

$$(\lambda + 2\mu) > \frac{4}{3}\mu > 0, \quad (\text{A16})$$

implying that

$$K_{\perp} > \frac{4}{3}K_{\parallel} > 0. \quad (\text{A17})$$

Since the thin layer we are considering is able to derive support from the adjacent media, it is not compelled to satisfy the normal bulk thermodynamic constraints. However, since we have little reason to anticipate abnormal mechanical properties of the layer material, we have confined most of our calculations, which we report on here, to values of the coupling constants that satisfy the inequality (A17).

In Sec. IV we have shown that the important parameters determining phonon scattering probabilities are

$$\alpha_{\parallel} = \frac{K_{\parallel} V_{ct}}{\mu_c \omega} = \frac{\mu}{h} \frac{V_{ct}}{\mu_c \omega} \lesssim 1, \quad (\text{A18})$$

and

$$\alpha_{\perp} = \frac{K_{\perp} V_{cl}}{(\lambda_c + 2\mu_c)\omega} = \frac{\lambda + 2\mu}{h} \frac{V_{cl}}{(\lambda_c + 2\mu_c)\omega} \lesssim 1, \quad (\text{A19})$$

the inequalities indicating the range of values consistent with experiment. The validity of the effective boundary conditions introduced here requires that

$$kh = \frac{\omega h}{V_t}, \quad \frac{\omega h}{V_l} \ll 1. \quad (\text{A20})$$

There is a limited frequency range that satisfies all the inequalities (A18)–(A20), namely

$$\frac{\mu V_{ct}}{\mu_c}, \quad \frac{(\lambda + 2\mu)V_{cl}}{\lambda_c + 2\mu_c} \lesssim \omega h \ll V_t, V_l. \quad (\text{A21})$$

The inequality (A21) demands in particular that

$$\rho V_t, \rho V_l \ll \rho_c V_{ct}, \rho_c V_{cl}, \quad (\text{A22})$$

i.e., the acoustic impedances of the boundary layer should be small compared to those of the crystal in order for these boundary conditions to be valid in the regime of small α_{\parallel} and α_{\perp} .

*Permanent address: Physics Department, University of Witwatersrand, Johannesburg, South Africa.

¹For reviews, see W. Eisenmenger, *J. Phys. (Paris) Colloq.* **42**, C6-201 (1981); J. P. Wolfe, *Phys. Today* **33**, (12) 44 (1980).

²G. A. Northrop and J. P. Wolfe, *Phys. Rev. Lett.* **43**, 1424 (1979); *Phys. Rev. B* **22**, 6196 (1980).

³W. Eisenmenger, in *Proceedings of the Third International Conference on Phonon Scattering in Condensed Matter*, edited by H. J. Maris (Plenum, New York, 1980), p. 303.

⁴R. Eichele, R. P. Huebener, H. Seifert, and K. P. Selig, *Phys. Lett.* **87A**, 469 (1982); R. Eichele, R. P. Huebener, and H. Seifert, *Z. Phys. B* **48**, 89 (1982).

⁵H. J. Maris, *J. Acoust. Soc. Am.* **50**, 812 (1971).

⁶A. K. McCurdy, H. J. Maris, and C. Elbaum, *Phys. Rev. B* **2**, 4077 (1970); B. Taylor, H. J. Maris, and C. Elbaum, *ibid.* **3**, 1462 (1971); J. C. Hensel and R. C. Dynes, *Phys. Rev. Lett.* **43**, 1033 (1979).

⁷F. Rösch and O. Weis, *Z. Phys. B* **25**, 101 (1976); **25**, 115 (1976).

⁸A. A. Kaplyanskii, V. A. Rachin, A. V. Akimov, and S. A. Basun, *Fiz. Tverd. Tela (Leningrad)* **23**, 488 (1981) [*Sov. Phys.—Solid State* **23**, 274 (1981)].

⁹M. Lax and V. Narayanamurti, *Phys. Rev. B* **22**, 4876 (1980).

¹⁰A. G. Every, *Phys. Rev. B* **24**, 3456 (1981).

¹¹P. Taborek and D. Goodstein, *Solid State Commun.* **33**, 1191 (1980); *Phys. Rev. B* **22**, 1550 (1980).

¹²D. Hurley, A. G. Every, and J. P. Wolfe (unpublished).

¹³G. L. Koos and J. P. Wolfe (unpublished).

¹⁴D. Marx and W. Eisenmenger, *Z. Phys. B* **48**, 277 (1982).

¹⁵W. E. Bron, M. Rossinelli, Y. H. Bai, and F. Keilman, *Phys. Rev. B* **27**, 1370 (1983).

¹⁶F. Rösch and O. Weis, *Z. Phys. B* **27**, 33 (1977); W. Kappus and O. Weis, *J. Appl. Phys.* **44**, 1947 (1973); O. Weis, *Z. Angew. Phys.* **26**, 325 (1969).

¹⁷S. Tamura and Y. Nakane, *Phys. Rev. B* **24**, 4317 (1981).

¹⁸These crystals are standard optical windows and were obtained

from Insaco Inc., Box 460, Quakerstown, PA 18951. The criterion for the quoted roughness is described in Sec. II.

¹⁹G. L. Koos, A. G. Every, G. A. Northrop, and J. P. Wolfe, *Phys. Rev. Lett.* **51**, 276 (1983).

²⁰M. J. P. Musgrave, *Crystal Acoustics* (Holden-Day, San Francisco, 1970).

²¹B. A. Auld, *Acoustic Fields and Waves in Solids* (Wiley, New York, 1973), Vol. 1.

²²F. I. Fedorov, *Theory of Elastic Waves in Crystals* (Plenum, New York, 1968).

²³It has been constructed by solving Cristoffel's equation for the grid of directions. A convenient method of solution is described by A. G. Every, *Phys. Rev. B* **22**, 1746 (1980); see also G. A. Northrop, *Comp. Phys. Commun.* **28**, 103 (1982) for a computer program for calculating acoustic phase and group velocities in crystals. Our illustrations make use of Northrop's software.

²⁴As long as the L sheet of the slowness surface remains detached from the other two sheets, it must be entirely convex. This has been proved by G. F. D. Duff, *Philos. Trans. R. Soc. London* **252**, 249 (1960).

²⁵W. E. Tefft, *J. Res. Nat. Bur. Stand. A* **70**, 277 (1966).

²⁶B. T. Bernstein, *J. Appl. Phys.* **34**, 169 (1963).

²⁷M. J. P. Musgrave, *Proc. R. Soc. London Ser. A* **226**, 339 (1954).

²⁸E. G. Henneke, *J. Acoust. Soc. Am.* **51**, 210 (1972).

²⁹G. W. Farnell, in *Acoustic Surface Waves*, edited by A. A. Oliner (Springer, Berlin, 1978).

³⁰The effect of interfacial species on shear strength of metal-sapphire contacts has been studied by S. V. Pepper, *J. Appl. Phys.* **50**, 8062 (1979).

³¹For an isotropic medium $C_{11} = \lambda + 2\mu$ and $C_{44} = \mu$, where C_{ij} are the conventional elastic constants. See J. F. Nye, *Physical Properties of Crystals* (Oxford University Press, London, 1957).

³²Our definition of emissivity differs from that used by Rösch

and Weis (Ref. 16). The latter relates the phonon power in the crystal to what it would be if the crystal were replaced by the metal and also incorporates the $\cos\theta$ factor. The relationship between their emissivity and ours is

$$\epsilon_{RW} = \frac{1}{\pi} \left[\frac{V_{mt}}{V_{ct}} \right]^2 \cos\theta \epsilon_{EKW}$$

for T phonons, and a similar expression holds for L phonons.

³³F. L. Becker and R. L. Richardson, in *Research Techniques in Nondestructive Testing*, edited by R. S. Sharp (Academic,

New York, 1970), p. 91.

³⁴R. E. Peterson and A. C. Anderson, *J. Low Temp. Phys.* **11**, 639 (1973).

³⁵A. C. Anderson, in *Nonequilibrium Superconductivity, Phonons and Kapitza Boundaries*, edited by K. E. Gray (Plenum, New York, 1981).

³⁶A. G. Eguluz and A. A. Maradudin, *Phys. Rev. B* **28**, 711 (1983); O. H. Duparc and A. A. Maradudin, *J. Electron. Spectrosc. Relat. Phenom.* **30**, 145 (1983).

³⁷V. R. Velasco and F. Garcia-Moliner, *Phys. Scr.* **26**, 405 (1982).

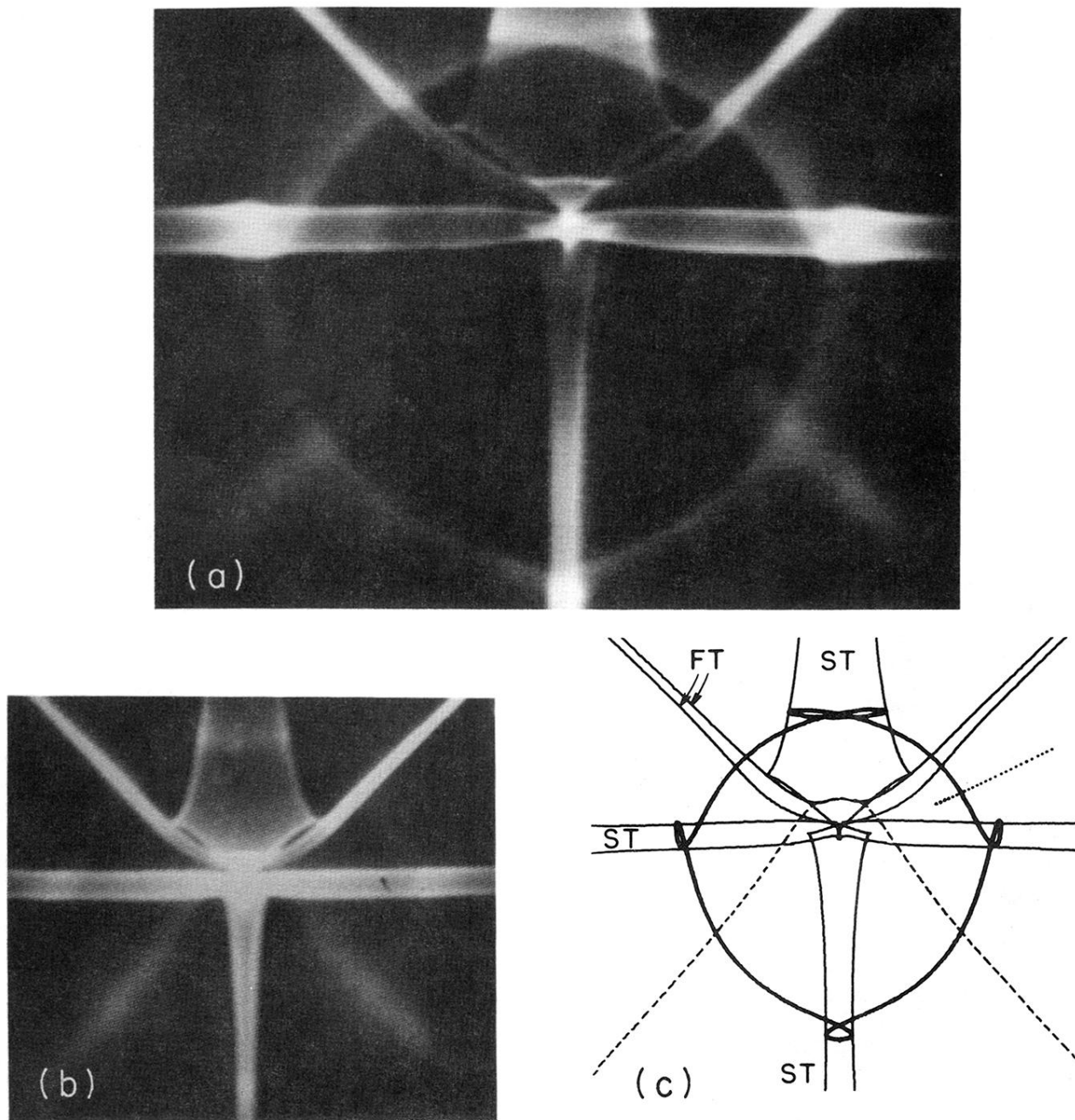


FIG. 1. (a) Ballistic phonon image for sapphire at 1.6 K. The detector and excitation faces are cut in the $[1\bar{1}02]$ direction, referred to conventional hexagonal axes, and both are highly polished. Bright regions indicate directions of high phonon flux. The image represents a $\pm 32^\circ$ horizontal scan with the $[1\bar{1}02]$ direction at the center of the pattern. The time gates of the boxcar integrator are set to accept the ST and FT modes. (b) Similar to (a) but with both faces of the sapphire roughened as described in the text (Sec. III). (c) Theoretical map of the caustics for sapphire projected onto the viewing surface of (a) and (b). The fast and slow transverse caustics are identified. The ST critical-cone channeling contour is given by the thick line. The scan line for Fig. 15 is indicated by the dotted line. The dashed line indicates the position of the precursor.

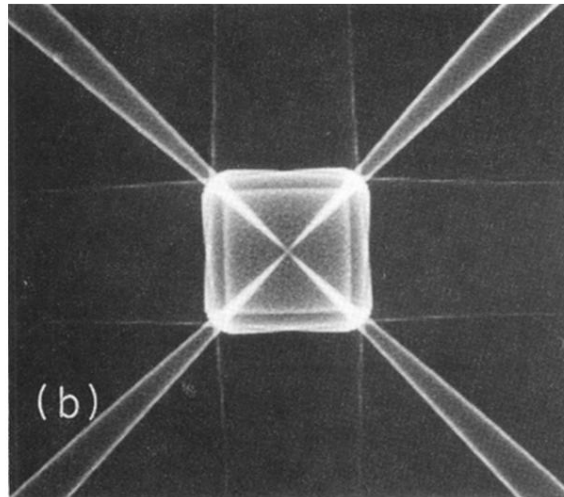
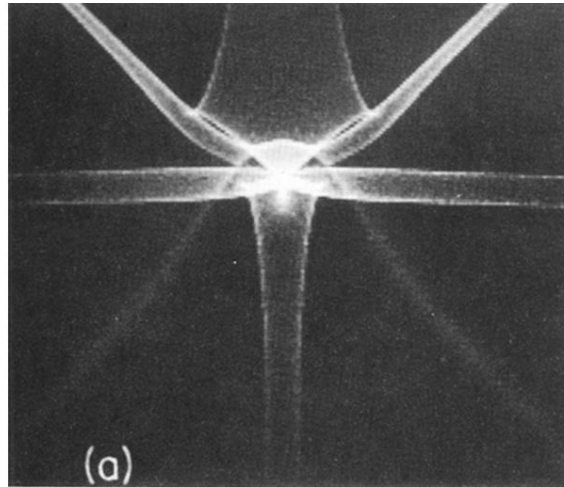


FIG. 4. (a) Monte Carlo calculation of the focusing pattern of sapphire for the same situation as in Fig. 1. This and later theoretical images are each composed of about 10^6 ray vectors. The computation requires about 20 min of CPU (central processing unit) time on a Digital Equipment Corporation computer VAX-11/750. (b) Monte Carlo image for germanium centered on the [100] direction. Interesting similarities can be seen between the images for sapphire and germanium.

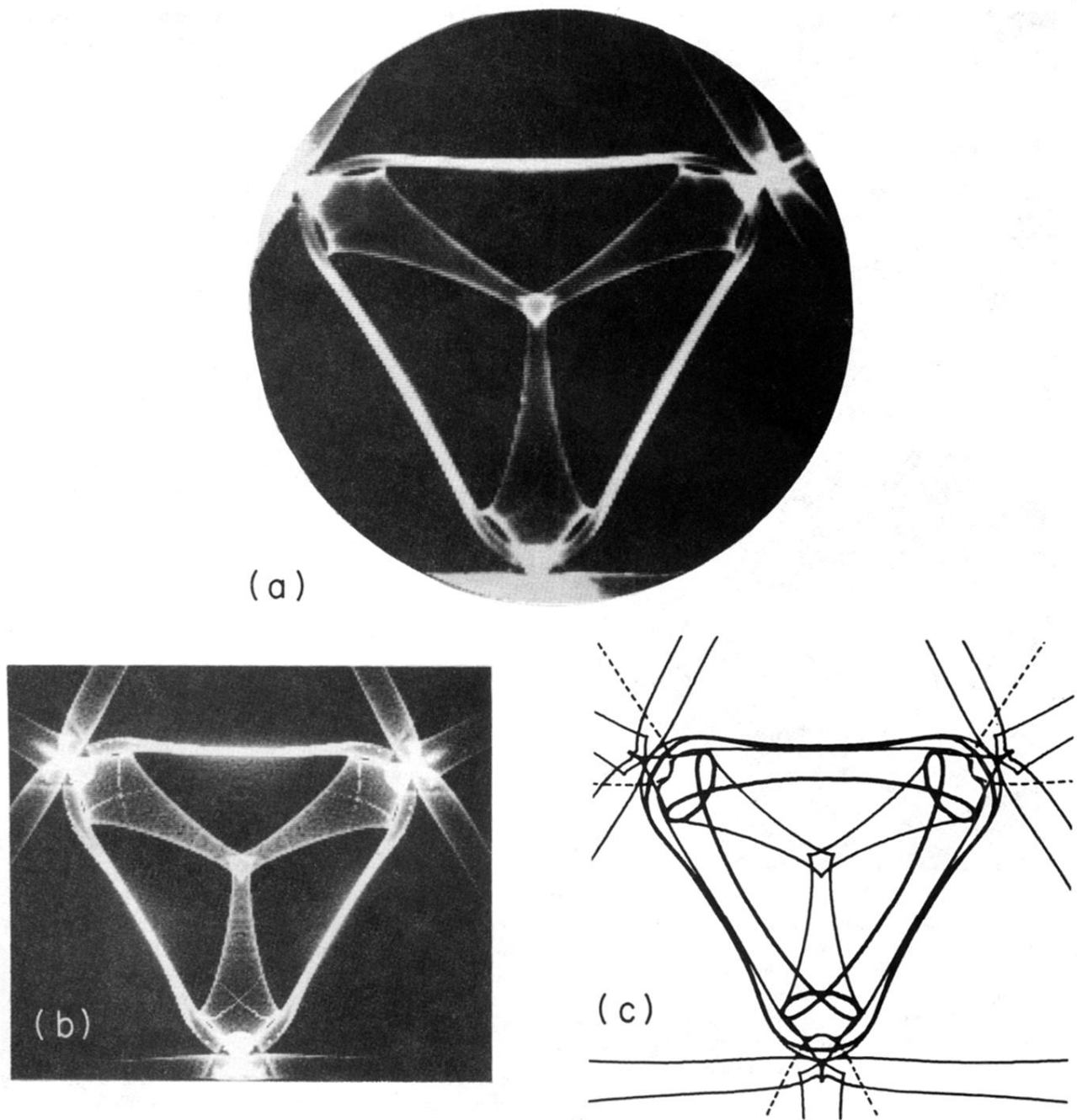


FIG. 5. (a) Experimental phonon image for sapphire with faces cut normal to the crystallographic c axis and polished. The image represents a radial scan of 58° . (b) Monte Carlo image for the same situation as in (a). The calculated critical-cone contours is denoted by the sequence of dots. The intensities of the dots are determined by the polarization condition discussed in the text. (c) Line drawings of the caustics and of the critical cone contours for the same orientation as (a) and (b).

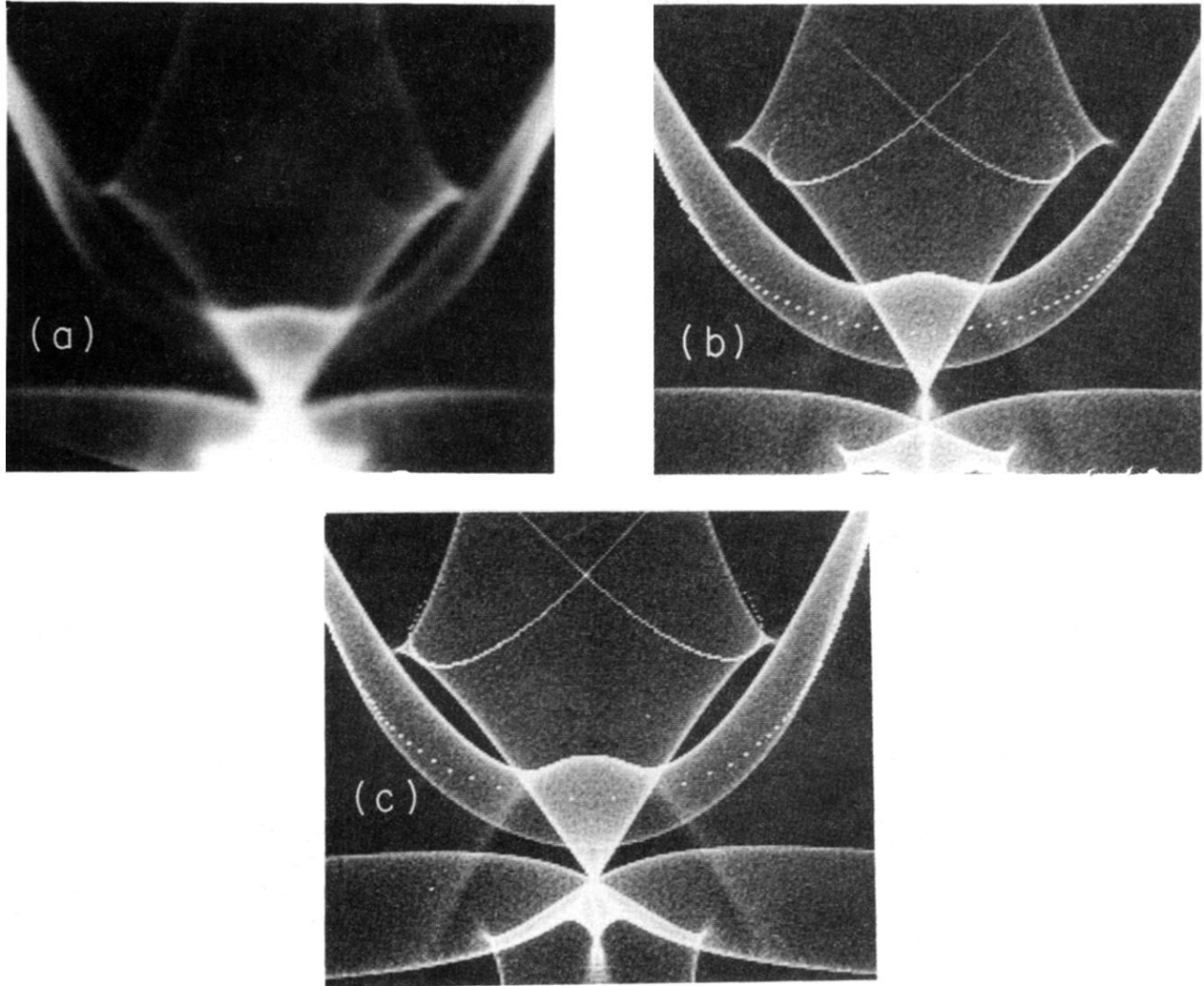


FIG. 6. (a) Enlargement of portion of the experimental phonon image of Fig. 5. (b) Theoretical image for the same situation as in (a), calculated with the elastic constant values $C_{11}=495.0$, $C_{12}=161.1$, $C_{13}=111.1$, $C_{14}=-22.2$, $C_{33}=499.9$, $C_{44}=147.7$, all in units of 10^{10} dyn/cm². These have been obtained by extrapolation to 2 K from values given in Ref. 25. (c) Theoretical image obtained using the elastic constant values $C_{11}=495.2$, $C_{12}=165.4$, $C_{13}=113.0$, $C_{14}=-23.2$, $C_{33}=493.2$, $C_{44}=148.8$, all in units of 10^{10} dyn/cm². These are low temperature values extrapolated from values given in Ref. 26.

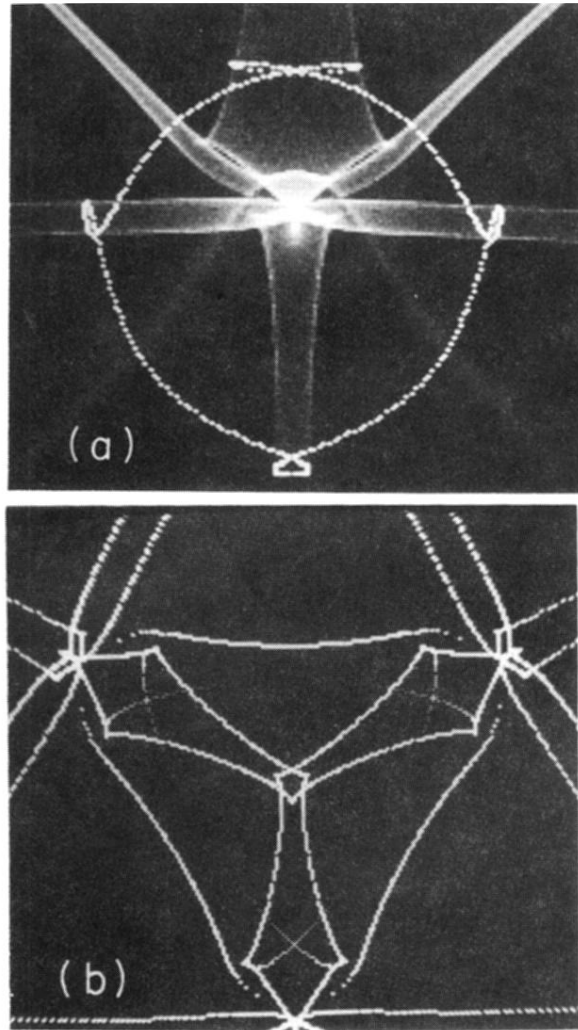


FIG. 8. (a) Monte Carlo image corresponding to Fig. 1. Critical-cone contours are shown by the sequence of dots, the intensity of which are determined by the polarization condition. (b) ST and FT critical-cone contours superposed on line drawing of ST caustics for the same situation as in Fig. 5.

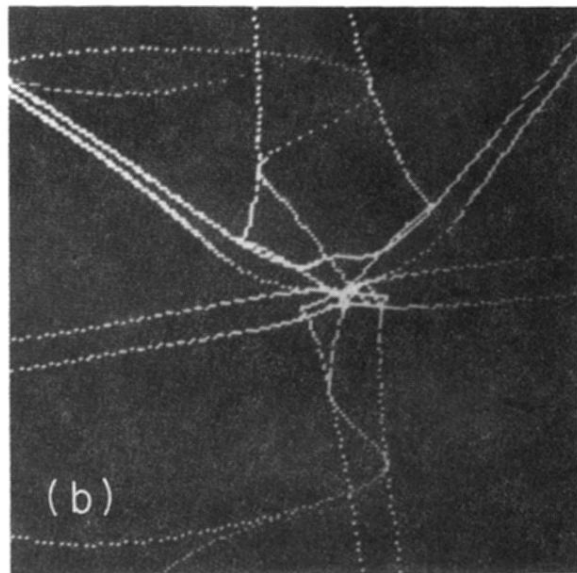
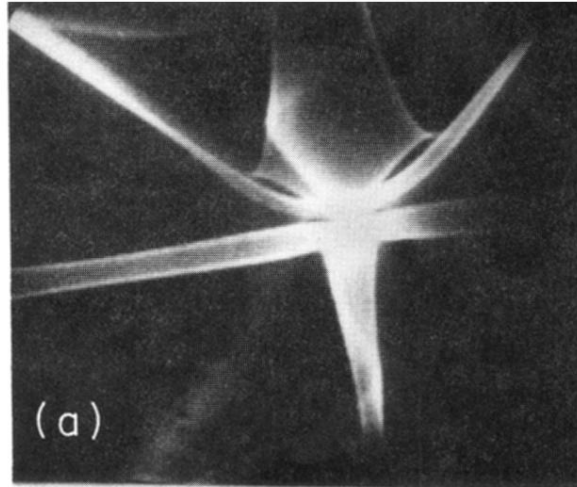


FIG. 9. (a) Experimental phonon image for sapphire with surfaces cut normal to the direction ($\theta=55^\circ$, $\phi=7^\circ$) and polished. (b) Line drawing of caustics and dotted critical-cone contours.